Study of Small Hydraulic Diameter Media for Improved Heat Exchanger Compactness

Antoine Corbeil

B. Eng., Mechanical Engineering, Royal Military College of Canada, 1995

A thesis submitted to the Faculty of Graduate and Postdoctoral Studies

in partial fulfillment of the requirements for the degree of

Masters of Applied Science

in Mechanical Engineering

Ottawa-Carleton Institute for Mechanical and Aerospace Engineering

Department of Mechanical Engineering

University of Ottawa

Ottawa, Canada

January 2011

ABSTRACT

Solar radiation offers phenomenal potential for energy conversion with energy densities on the order of 1000W/m^2 in locations with regularly clear skies. As always, the difficulty lies in finding a solar-electric conversion technology capable of producing electricity at a competitive cost. The SolarCAT (Solar Compressed Air Turbine) system produces electricity by releasing stored compressed air through a series of turbines with solar dish concentrators providing the required heat for efficient conversion to electricity. To minimize impact on capital cost, high recuperator effectiveness targets are sought but unlike typical fuel-fired micro-turbines, raising the recuperator effectiveness of the solar power system yields a benefit in overall system capital cost. Improving efficiency lowers the size and cost of the largest element of the system, namely the dish.

In this study potential techniques for achieving a highly compact heat-transfer media were reviewed. Folded fin, packed beds, micro-tubes, lattice frame structures, metal foams, woven textile, and micro-machining techniques were assessed. Textile structures were selected as an appropriate medium to replace the internal folded fin of the SolarCAT recuperator. The relatively long flow (>150mm) path through the proposed screen wafers requires a model for fully-developed forced convective flow between parallel plates. A mathematical model was developed by integrating the results from the work of several authors in the field of textiles and porous media. #100 mesh sintered screen wafers were brazed between two 0.25mm stainless steel sheets and destructively tested to assess their tensile strength. Although

optimization of the braze parameters was not completed, it was found that many samples survived exposure to internal pressures in excess of 50MPa.

This study found that the use of sintered screen wafers to replace the internal folded fin of the SolarCAT recuperator would have advantages over the current design with respect to both overall recuperator effectiveness, size, and cost. Textile structures can be tailored to have wide range of fluid and heat-transfer properties depending on the application. The manufacturing process is relatively simple and could be cost-effective for high-volume production.

ACKNOWLEDGMENTS

The author would like to thank Bertrand Jodoin for providing guidance and advice throughout this endeavour. Thanks to Professor Rich Wirtz at the University of Nevada, Reno for sharing his expertise in this field. In addition, the author is grateful to Jim Kesseli, Jim Nash and the team from Brayton Energy, LLC for this incredible opportunity and their ongoing support. Kind regards to colleagues and fellow students Grégoire Bérubé and Eric Matte for their assistance.

Finally, the author would like to thank his family and friends for their never-ending encouragement and would like to dedicate his thesis to his beautiful wife and daughters:

Anik, Vanessa, Daphne and Sophie

You mean everything to me.

Table of Contents

LIST OF TABLES

LIST OF FIGURES

1. INTRODUCTION

1.1 Background

1.1.1 Trends in Power Generation

Currently, there is tremendous social and political pressure to reduce emissions and fuel utilization in almost every industry. Power generation is certainly not an exception. There is a push to find effective renewable/regenerative energy solutions and a general trend towards deregulation of global electric energy markets. Combined Heat and Power (CHP) solutions, where power is produced and waste heat from the exhaust is recuperated for useful purposed, have great potential in many areas and are becoming more and more accessible due to developments in distributed power generation.

With this distributed approach energy losses due to long-distance transmission are reduced and there is a reduced risk of widespread electrical failure as a result of the proximity of power generation to the end users. In essence, a plant could produce electricity for their needs and potentially sell the excess back to the grid. Micro-turbines are critical to the success of distributed power generation.

1.1.2 Compact Generators

Micro-turbines are compact gas-turbine generator systems that use liquid or gaseous fuel to produce electricity and heat. Manufacturers offer commercially available units from 25kW to

250kW with systems up to 500kW currently being planned or developed. The novelty of the micro-turbine is in its simplicity. With few mechanical components, low emissions, decent efficiency and a compact package, they are perfect for distributed power applications.

1.1.3 Simple and Recuperated Cycles

As shown in Figure 1-1, in its simplest form, a micro-turbine is a simple-cycle gas-turbine system that consists of a single shaft, compressor (typically centrifugal), a combustion chamber, a turbine (typically radial flow), and a permanent magnet alternator. Electrical net efficiencies for the simply cycle micro-turbines are often less than 20% but this can be significantly improved with the addition of a heat-exchanger, as shown in Figure 1-2, called a recuperator to the point where systems commonly demonstrate electrical net efficiencies of over 30%. Thermal efficiency is simply the ratio work extracted from a system to total heat input to the system. Electrical net efficiency applies a decrement to thermal efficiency to account for the losses incurred to produce electricity. The losses include mechanical losses due to gears, losses in electronics, etc. They typically represent a few percent of the power output.

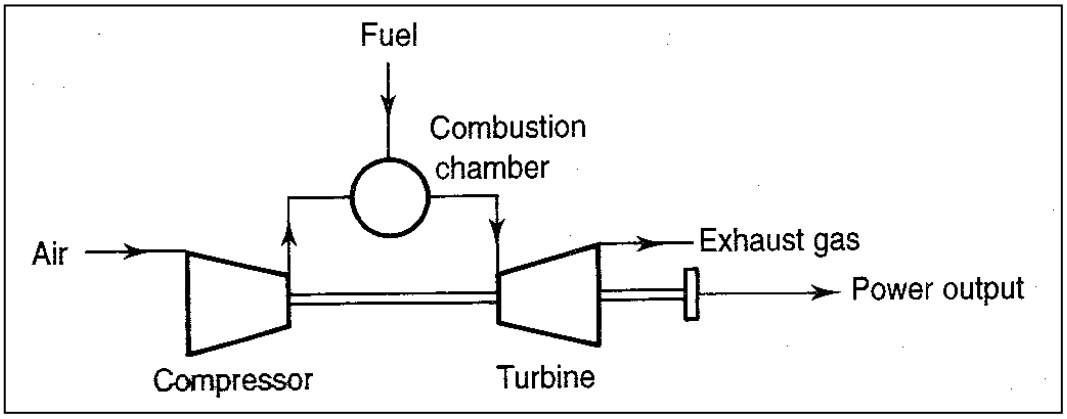

Figure 1-1 [1] Simple Open Cycle Gas Turbine System

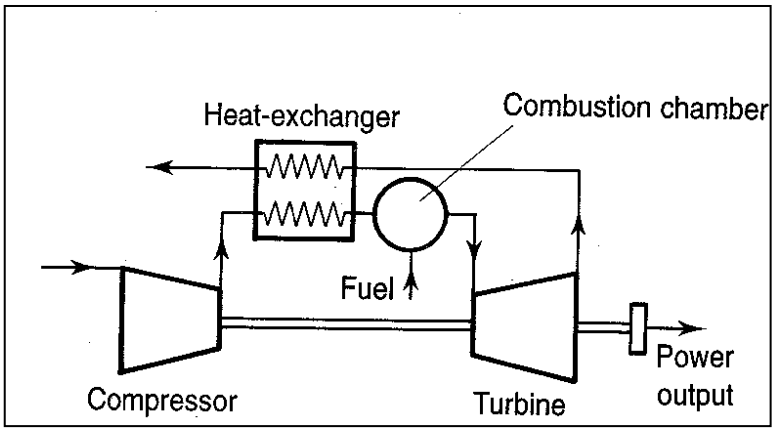

Figure 1-2 [1] Single-shaft Open Cycle Gas Turbine with Heat-exchanger

1.1.4 Efficiency Limitations and Combined Heat and Power (CHP)

In comparison with larger, multi-stage, multi-shaft gas turbines, micro-turbines have low efficiencies. Diesel and gas reciprocating engines are the principal competitors to micro-turbines in the distributed power market. Thermal efficiency of the reciprocating engines is most often higher (see Figure 1-3) than that of the micro-turbines but their waste heat is difficult to use or tied up in engine cooling. A great deal of research ("projects" in Figure

1-3) is being done to improve gas-turbine efficiencies, including work done by Kawasaki Heavy Industries (KWI) into the use of ceramics for hot-end components in order to increase turbine inlet temperatures and thereby improve thermal efficiency.

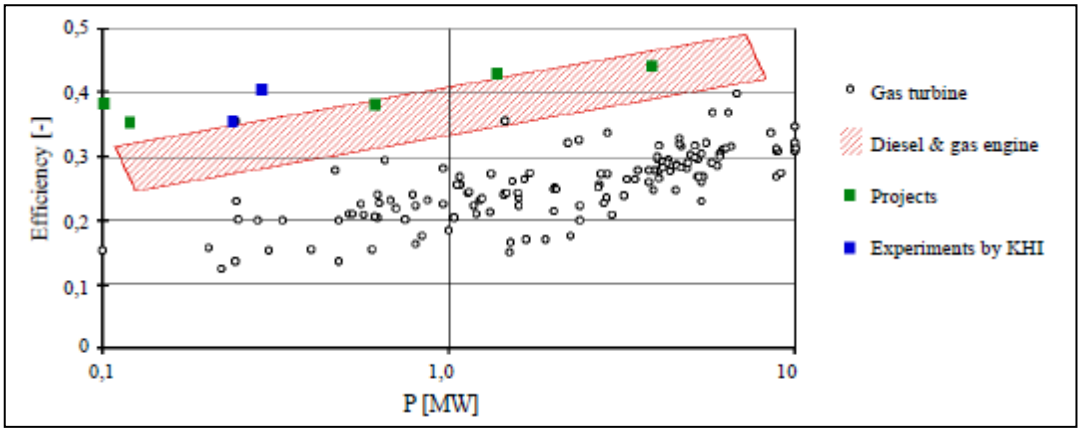

Figure 1-3 [2] Comparison of Gas Turbine and Reciprocating Engine Efficiencies

However, in general, due to their lower efficiencies it is important to consider the use of waste heat from the micro-turbine for combined heat and power applications. Extracting heat is done by inserting a heat exchanger in the micro-turbine exhaust stream to use the heat for required plant processes, local heating, cooling through an absorption chiller, or local hot water. In this manner, thermal efficiency for CHP systems is often in the range of 80%.

Advances in micro-turbine design will lead to higher micro-turbine thermal efficiencies with improvements in all turbine components and improved recuperator effectiveness at higher temperatures and pressures. The timeline shown in Figure 1-4 is clearly optimistic but it shows that micro-turbines have the potential to operate at thermal efficiencies very close to those of the reciprocating engines in the near future.

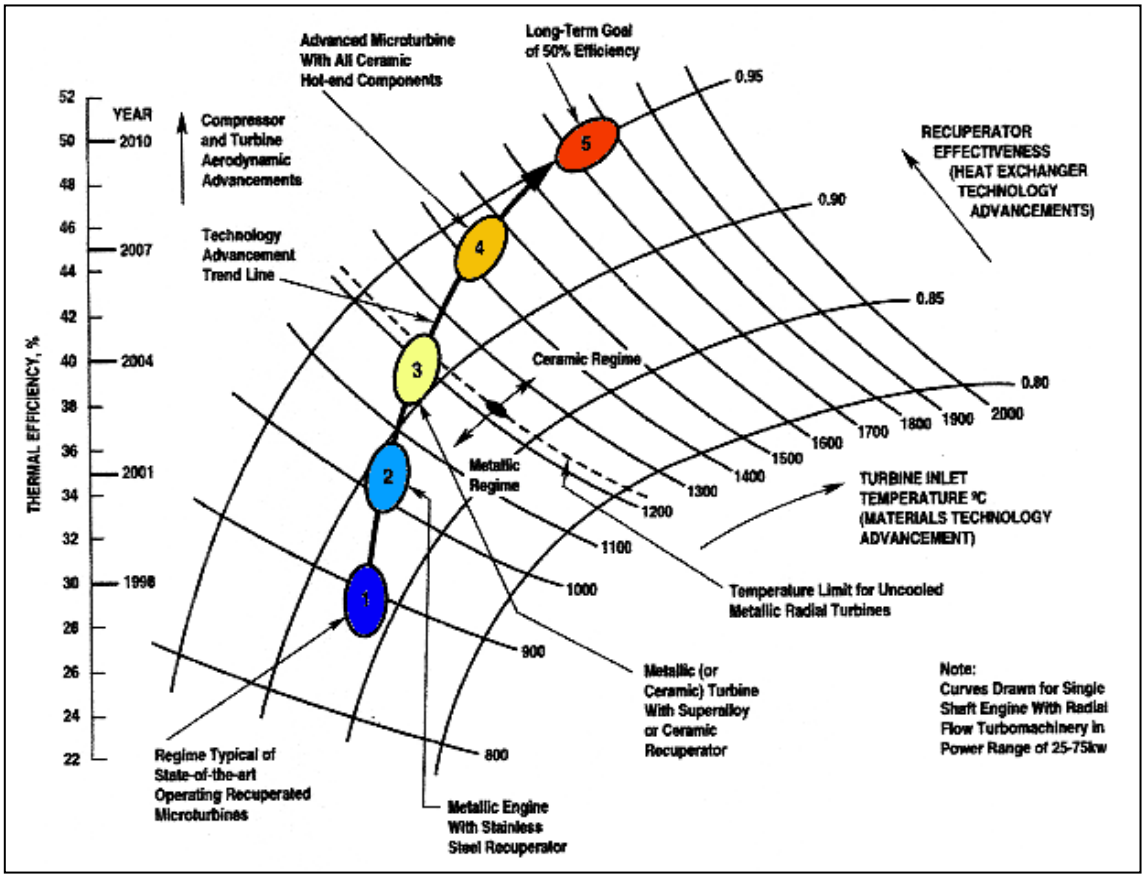

Figure 1-4 [2] Predictions in Mirco-turbine Development

1.1.5 Importance of a Recuperator

The micro-turbine recuperator is a critical, complex and costly component. At this time, most recuperators used in the industry are of the counter-flow variety and are designed for about 85% to 90% effectiveness. Heat-exchanger effectiveness is the ratio of heat transfer rate transferred from one fluid to the second to the maximum possible heat transfer rate. As a result of high target effectiveness, the volume of the heat-exchanger is quite large. Volume and cost are closely tied, as heat-exchanger volume has a direct impact on the quantity of material required. As seen in Figure 1-4, improvements in micro-turbine thermal efficiency will require an additional 5-10% increase in recuperator effectiveness.

Heat Capacity rate ratio (C*) is the ratio of minimum to maximum capacity rates of the two fluids in the heat exchanger. A balanced heat exchanger has a C* of 1.

$$C^{\times} = \frac{C_{min}}{\mathrm{C_{max}}} = \frac{(\dot{m}\, C_P)_{min}}{(\dot{m}\, C_P)_{max}} \tag{1.1}$$

Given that a micro-turbine's inlet massflow typically differs from its outlet massflow only by the addition of fuel in the combustion chamber and C_P changes only slightly over the temperatures in question, C* is almost always very close to balanced. As can be seen from Figure 1-5, at 90% effectiveness and C* of 1, a large increase in the number of transfer units (non-dimensional thermal size of the heat-exchanger) is required for a small increase in heat exchanger effectiveness. Overall system performance calls for the highest possible heat-exchanger effectiveness. Recuperator cost increases with recuperator volume. The cost of a typical micro-turbine recuperator is roughly 20-25% of the total micro-turbine generator set cost [3] and it occupies about 20-35% of the overall package volume. As the industry strives for better overall system performance, recuperator designers must greatly improve compactness.

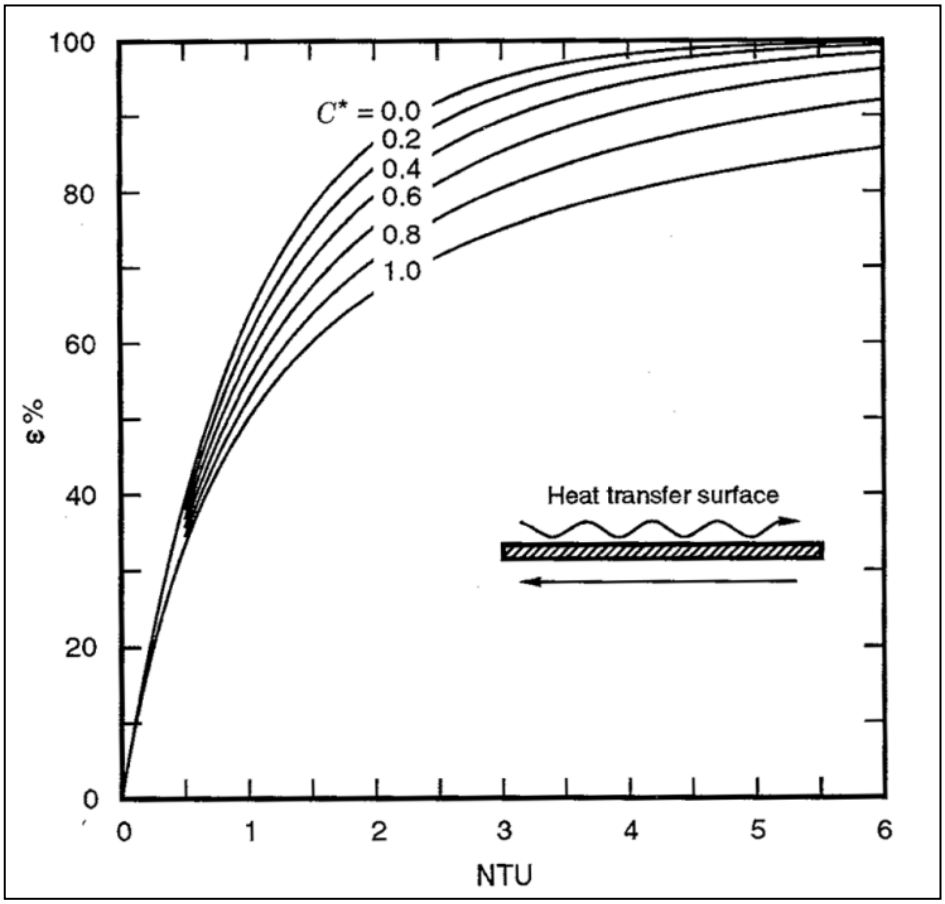

Figure 1-5 [4] Counterflow Heat Exchanger ε as a Function of NTU and C*

1.2 Motivation of Study and General Objectives

1.2.1 Harnessing Solar Energy – Basic Principles of the SolarCAT

Solar radiation offers phenomenal potential for energy conversion with energy densities on the order of 1000W/m^2 in locations with regularly clear skies. As always, the difficulty lies in finding a solar-electric conversion technology capable of producing electricity at a competitive cost. Brayton Energy, LLC put forward a solar conversion system concept where economic considerations were of primary importance. Initial and operating costs need to be substantially lower than those of competing solar technologies, and in-line with more conventional power-generation systems. Hardware proven in industrial gas-turbine settings will offer high reliability and there is potential for energy storage load-following. This concept was named SolarCAT (Solar Compressed Air Turbine).

During off-peak (night-time) periods, compressed air is produced with an industrial compressor using available low-cost electricity and stored in underground geologic reservoirs (salt domes) or in pressure vessels fabricated with inexpensive commodity piping.

During peak periods (daytime), electricity is produced by releasing the stored compressed air through a series of turbines with solar dish concentrators providing the required heat for efficient conversion to electricity. An array of dish/turbine modules are planned with a centralized facility providing compression/storage capabilities. If the compression and expansion were to occur at the same time, the cycle would be that of a typical gas-turbine.

1.2.2 SolarCAT Recuperator

As stated earlier, for a gas-turbine system, increased recuperator effectiveness improves efficiency and therefore power with respect to a given thermal input. In this case, recuperator effectiveness (ε) has an additional benefit in the form of reduced dish area for a desired power. In this case, the incentive for high ε is particularly strong.

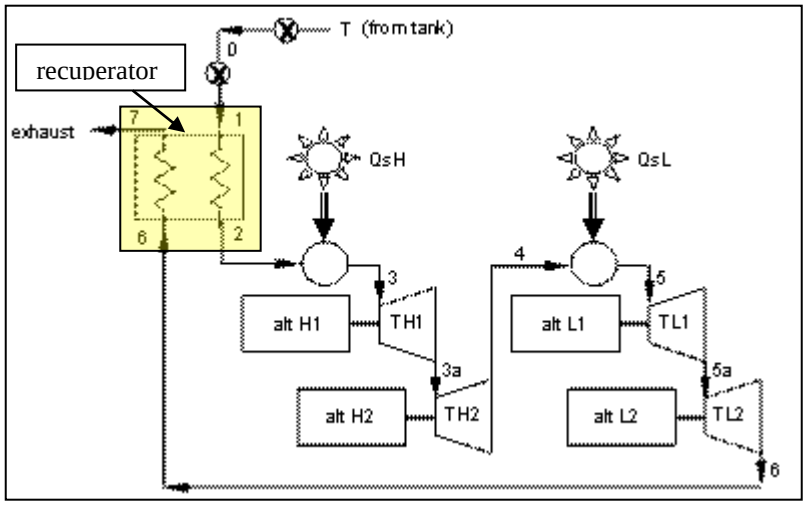

Figure 1-6[Brayton Energy, LLC] SolarCAT Schematic

To minimize impact on capital cost, high recuperator effectiveness targets are sought but unlike typical fuel-fired micro-turbines, raising the recuperator effectiveness of the solar power system yields a benefit in overall system capital cost. Improving efficiency lowers the size and cost of the largest element of the system, namely the dish. The relatively modest increment in system cost for the increased effectiveness recuperator allows for specification of a smaller concentrator dish, creating net cost avoidance.

Due to a number of design considerations, including the need to limit recuperator inlet temperature at part-load conditions, a higher than optimum overall cycle pressure ratio was selected, leading to a recuperator inlet air pressure of 2.2MPa. Although the pressure is quite high, the temperature (880K) is relatively low for a micro-turbine recuperator.

The recuperator is a proprietary design developed by Brayton Energy, LLC. The high pressure of the SolarCAT cycle allows for a very compact design but presents many challenges with respect to its structure. The novel design is a counter-flow plate-fin heat exchanger with structural features to accommodate the high pressures of this application. The high performance target (94% effective vs. 85-90% typical) is easier to achieve at high pressures as the internal, pressurized fluid occupies less volume and requires less frontal area. This leads to a smaller heat-exchanger and lower cost, as less material and labor are required. Alloy-347 stainless steel was selected for all recuperator components due to the moderate temperatures and the low water content of the compressed/cooled air. The SolarCAT recuperator design points allow for the use of less exotic materials, thereby lowering the cost and ensuring adequate life for the product.

1.2.3 SolarCAT Recuperator Manufacturing Limitations

Although all the decisions taken in the design of the recuperator should lead to a low-cost product, a manufacturing limitation made it impossible to take full advantage of the favourable design criteria. Mechanical fin folding is used to create extended heat-transfer surface area on either side of a pair of stamped plates. This design consists of a single high-pressure fin captured between symmetric stamped plates with low-pressure extended surface

on the both outermost plate faces (Figure 1-7). Micro-turbine recuperator pressure loss budgets are typically 2-3% of inlet pressures for both high and low pressure fluids.

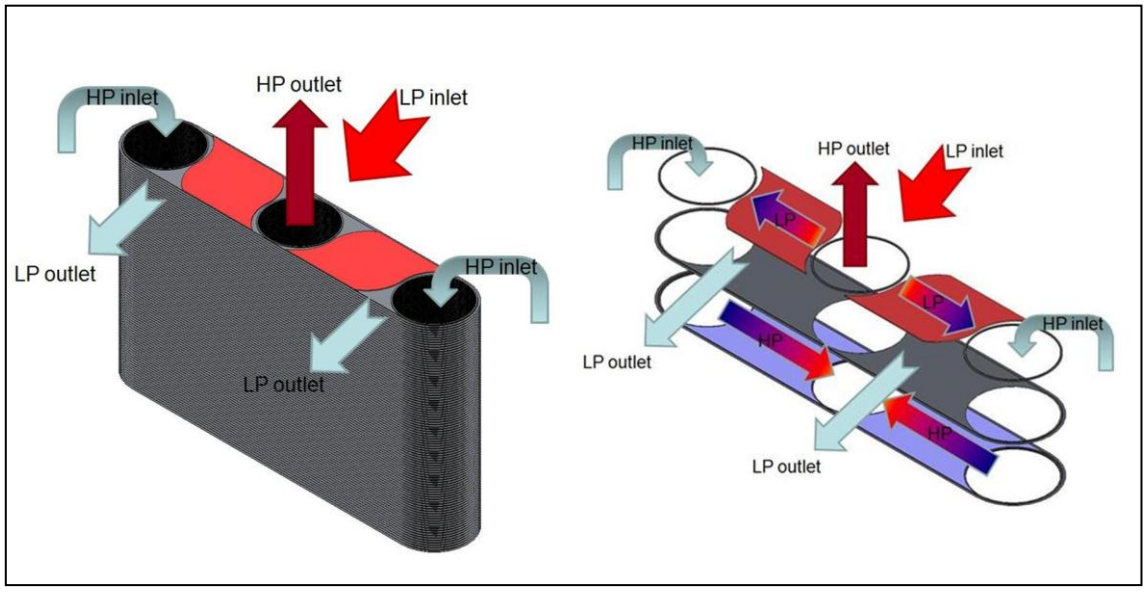

Figure 1-7 [Brayton Energy, LLC] SolarCAT Recuperator Unit Cell

In this case, the internal pressure was such that for a reasonable external fin design, fin folding could not create a fin with sufficiently small hydraulic diameter to take full advantage of the pressure-loss budget. Using 0.1mm thick alloy-347 stainless steel with a fin height of 0.89mm, the maximum fin fold density (number of folds per unit length) for a ruffled fin was determined to be 1693 fins per meter [Robinson Fin Machines, Inc.]. Compact heat-exchangers typically incorporate heat-transfer surfaces with hydraulic diameters between 1mm and 6mm [4]. With a hydraulic diameter of 0.68mm, this fin is quite compact but still much too large to take advantage of the very high internal pressure. The principal objective of this study is to identify a small hydraulic diameter medium capable of replacing the existing SolarCAT recuperator internal fin in order to improve compactness of the heat-exchanger.

2. REVIEW OF RELEVANT LITERATURE

2.1 Basic Function of Heat Exchangers

The goal of a heat exchanger is to transfer thermal energy from one fluid stream to another. This can be accomplished in many different ways but there is always one fluid that is considered the "hot" fluid and one that is the "cold" fluid. When observing a gas-turbine recuperator, the hot fluid is the turbine exhaust and the cold fluid is the compressor discharge air (see Figure 1-2).

2.1.1 Thermal Conductance

For a typical two fluid heat-exchanger, Figure 2-1 illustrates the convective and conductive mechanisms in the overall heat transfer rate equation. The term $\frac{dq}{dA}$ is the heat flux for a unit heat transfer area and U is the thermal conductance term for a temperature potential from t_h to t_c.

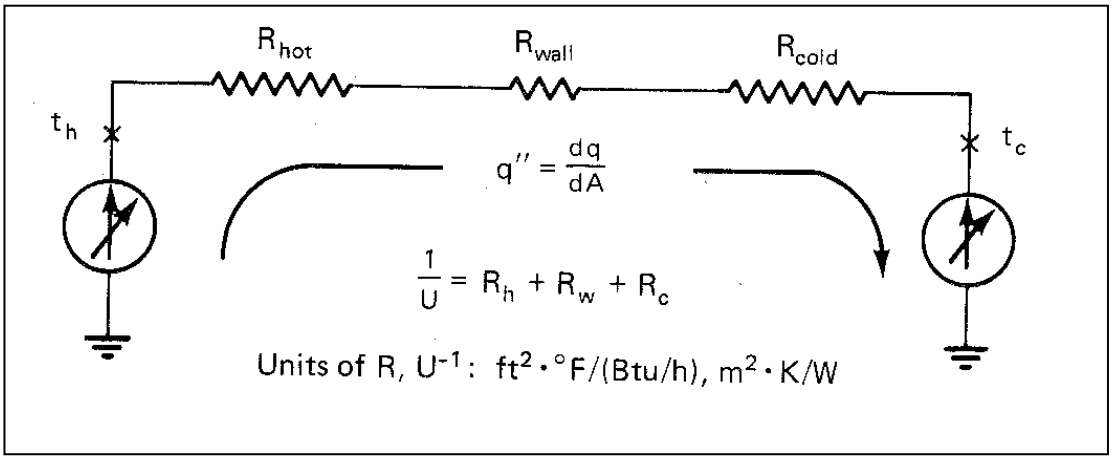

Figure 2-1 [5] Thermal Circuit Representation

This general representation is adequate to analyze the vast majority of conventional direct-transfer, two fluid heat-exchangers. The overall heat-transfer rate equation is as follows:

$$dq = U\ (t_h - \ t_c)\ dA \tag{2.1}$$

The overall thermal resistance, $\frac{1}{U}$, is composed of three basic terms:

$$\frac{1}{U} = \ R_{conv-hot} + R_{cond} + R_{conv-cold} \tag{2.2}$$

1. Hot-side convective heat-transfer term;
2. Wall conductive heat-transfer term;
3. Cold-side convective heat-transfer term.

Both convective terms are a function of the convective heat-transfer coefficients (h), the total heat-transfer area (A, including extended surface area), and temperature effectiveness of the total heat-transfer area (η_o). The conductive term is simply a function of the wall thickness (δ), its heat-transfer surface area (A_{wall}), and the material conductivity (k).

$$R_{conv} = \frac{1}{\eta_o\ h\ A} \tag{2.3}$$

$$R_{cond} = \frac{\delta}{A_{wall}\ k} \tag{2.4}$$

Determination of the hot and cold side heat-transfer areas and temperature effectiveness terms can be quite challenging if there is extended surface (fins, etc.) with complicated geometry. Also, equations for heat transfer coefficients will vary with geometry.

2.1.2 Effectiveness and the Number of Transfer Units Method

The heat transfer rate, q, from the hot fluid to the cold fluid is given by:

$$q = \varepsilon C_{min} \left(T_{h,i} - T_{c,i}\right) = \varepsilon C_{min} \Delta T_{max} \tag{2.5}$$

Where ε, heat-exchanger effectiveness is the ratio of actual heat transfer rate to maximum possible heat transfer rate as follows:

$$\varepsilon = \frac{q}{q_{max}} \tag{2.6}$$

where C_{min} is the lesser of C_h and C_c.

$$q_{max} = C_{min} \Delta T_{max} \tag{2.7}$$

This gives us a general equation for heat-exchanger effectiveness:

$$\varepsilon = \frac{q}{q_{max}} = \frac{C_h \left(t_{h,in} - t_{h,out}\right)}{C_{min} \left(t_{h,in} - t_{c,in}\right)} = \frac{C_c \left(t_{c,out} - t_{c,in}\right)}{C_{min} \left(t_{h,in} - t_{c,in}\right)} \tag{2.8}$$

The number of transfer units (NTU) is defined as the ratio of overall thermal conductance to the minimum heat capacity rate as follows:

$$NTU = \frac{A\,U_{av}}{C_{min}} = \frac{1}{C_{min}} \int_0^A U\,dA \tag{2.9}$$

where A is the area that is used in the definition of the overall conductance term, U. Typically, effectiveness will increase asymptotically with increasing NTU to a maximum effectiveness that is a function of the capacity rate ratio, C* (eqn. 1.1) and the heat-exchanger's flow arrangement.

2.1.3 Heat Exchanger Flow Arrangements

Heat exchangers can be arranged in a vast number of arrangements to accommodate integration into the surrounding systems. Concentrating on direct-transfer systems, there are only three basics approaches for the two fluids involved but these approaches can be combined to provide an endless number of possibilities. Typically, the objective is to aim for a large temperature gradient which will improve performance and reduce size.

2.1.3.1 Parallel Flow Arrangement

In a parallel flow exchanger, both fluids flow in the same direction and are parallel to one another (see Figure 2-2). As a result, there is a very large temperature difference at the inlet and a very small difference at the outlet. The rapidly decreasing temperature potential leads to lower effectiveness but there are often integration benefits that sometimes make this configuration attractive.

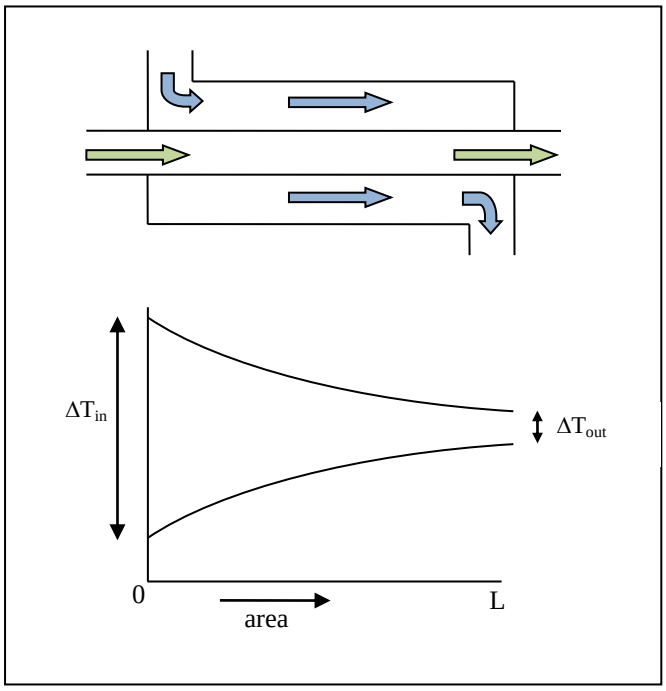

Figure 2-2 Parallel Flow Schematic and Temperature Distribution

2.1.3.2 Counterflow Arrangement

The counterflow arrangement is more effective than all other heat exchanger flow arrangements [4]. The initial temperature potential is smaller than that of a parallel flow exchanger but it remains relatively constant over the entire length (see Figure 2-3). The only drawback is that integration is sometimes difficult as the two flows must be directed in opposite directions, which may cause complications with headers and sealing. Ultimately, if the system layout can accommodate the use of a counterflow heat-exchanger, this arrangement will produce the most compact heat-exchange core (excludes headers).

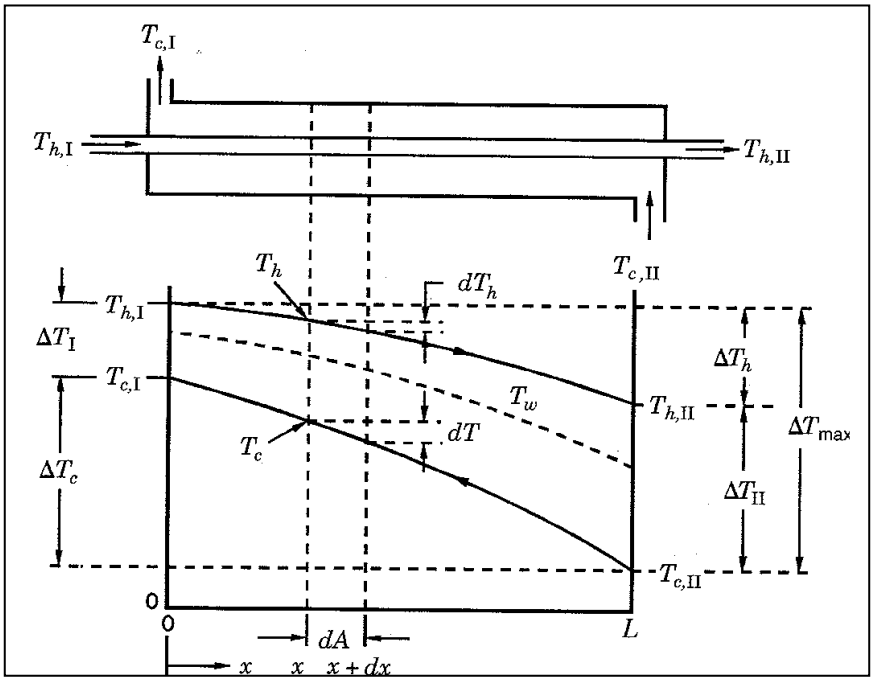

Figure 2-3 [4] Counterflow Schematic and Temperature Distribution

2.1.3.3 Cross-Flow Arrangement

Often, the simplest mechanical arrangement favours the use of a cross-flow heat-exchanger, where the two fluids are perpendicular. An example of this configuration is the automobile radiator. Air flow from vehicle's movement is allowed to pass through the heat-exchanger to cool the engine's coolant fluid.

Even parallel and counterflow arrangements often require that one flow be turned at some point to achieve the desired configuration. The region that turns the flow is often called a header. Headers are flow guides that turn the flow from its initial trajectory to a parallel or counterflow arrangement. There is almost always a portion of a heat-exchanger that can be considered to be cross-flow. Figure 2-4 illustrates a typical counterflow plate-fin

arrangement. The green arrows represent internal (pressurized) flow and the blue arrows represent external (low-pressure) flow. The pink regions are headers that turn the internal flow from cross-flow to counterflow. The matrix region shown in orange is pure counterflow. This arrangement is referred to as counterflow with cross-flow headers.

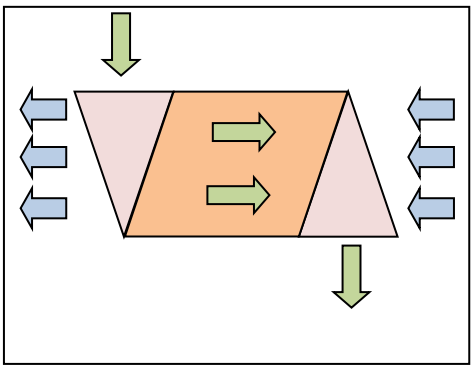

Figure 2-4 Counterflow Heat Exchanger with Cross-flow Headers

Cross-flow effectiveness lies somewhere between that of a parallel and a counterflow heat-exchanger. Often a cross-flow arrangement will require more area to achieve the desired effectiveness target. A solution is to have one flow cross the other flow many times thereby increasing the total heat-transfer area. This is referred to as a multi-pass cross-flow arrangement. The improvement in effectiveness is most often accompanied by an increase in weight and complexity of the system. Multi-pass configurations can be divided into two separate categories:

1. Cross-flow, overall counterflow
2. Cross-flow, overall parallel flow

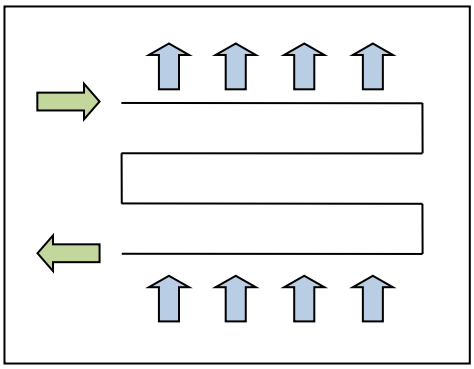

Figure 2-5 Cross-flow Overall Counterflow

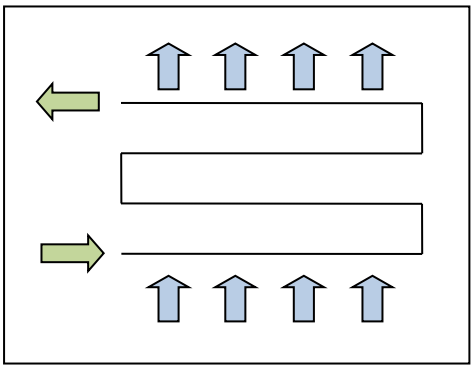

Figure 2-6 Cross-flow Overall Parallel Flow

2.1.4 Pressure Losses

Effectiveness and pressure losses are critical performance criteria for gas-gas heat exchangers. These terms are most often specified prior to initial sizing and will control the volume and frontal area of a design. Because of the importance of frictional losses in low-density fluids, determination of the flow-friction factor, *f*, which varies with geometry and Reynolds number, is vital to the design process.

Figure 2-7 illustrates several aspects of pressure loss through a typical unit cell of a plate-fin heat-exchanger. The process can be separated into three distinct regions. From station 1 to station 2, the flow contracts as there is less open frontal area at the entrance of the heat-exchanger, followed inevitably by flow separation. The second region is within the core (*matrix*), from station 2 to station 3, where the flow experiences frictional effects, form drag (if there is an interrupted extended surface), internal contractions and expansions, and changes in fluid density and velocities due to temperature changes through the matrix. Lastly, from station 3 to station 4, the flow exits the matrix where there is flow separation followed by an expansion due to increasing free-flow area.

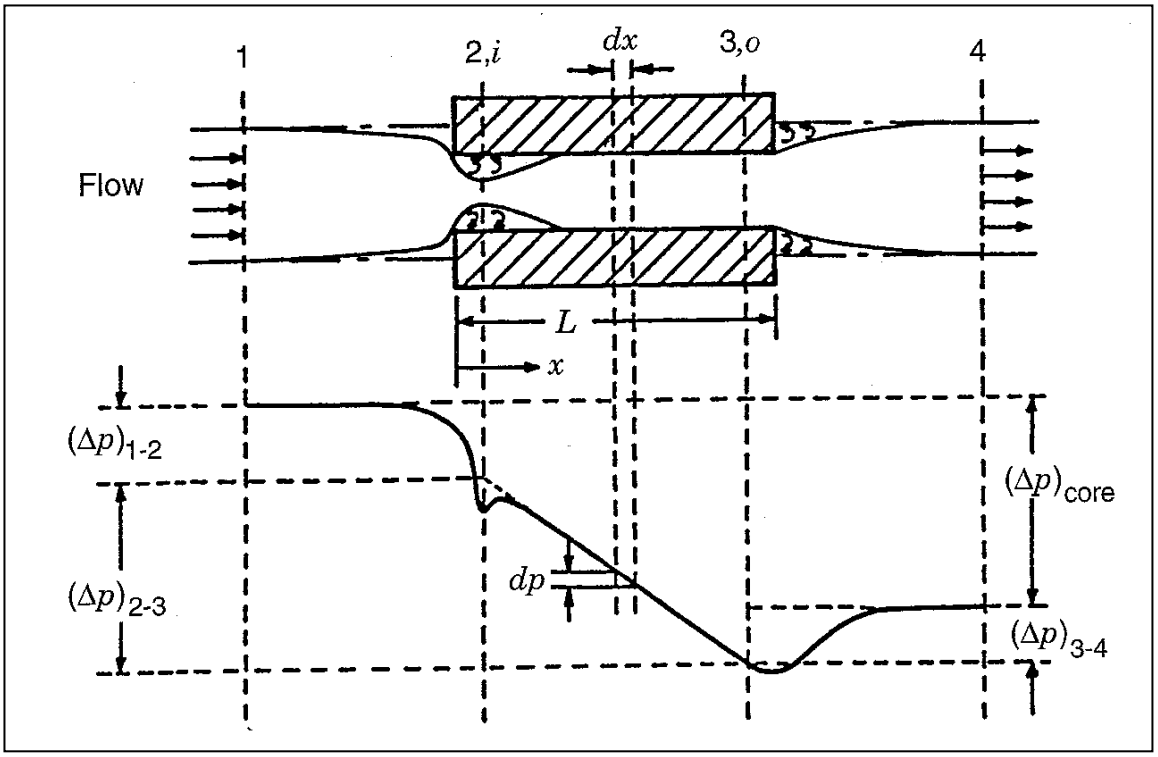

Figure 2-7 [4] Pressure Drop Components in a Single Cell of a Typical Plate-fin Heat-exchanger

Total pressure drop through the heat-exchanger is simply the sum of the pressure drops in each distinct region:

$$\Delta P = \Delta P_{1-2} + \Delta P_{2-3} + \Delta P_{3-4} \tag{2.10}$$

Matrix pressure drop:

$$\Delta P_{2-3} = \frac{G^2}{2\, g_c \rho_i}\left[2\left(\frac{\rho_i}{\rho_0} - 1\right) + f\,\frac{L}{r_h}\rho_i\left(\frac{1}{\rho}\right)_m\right] \tag{2.11}$$

Entrance pressure drop:

$$\Delta P_{1-2} = \frac{G^2}{2\, g_c \rho_i}(1 - \sigma^2 + K_c) \tag{2.12}$$

Where σ is the ratio of free-flow area at station 2 over the area at station 1 and K_c is the entrance loss coefficient. G is the matrix mass velocity ($\frac{\dot{m}}{A_0}$).

Exit pressure rise:

$$\Delta P_{3-4} = \frac{G^2}{2\, g_c \rho_i}(1 - \sigma^2 - K_e) \tag{2.13}$$

Where σ is the ratio of free-flow area at station 3 over the area at station 4 and K_c is the entrance loss coefficient. Kays and London [5] also define the flow stream pressure-drop calculation in the same manner:

$$\frac{\Delta P}{P_1} = \frac{G^2}{2\, g_c}\frac{v_1}{P_1}\left[(K_c + 1 - \sigma^2) + 2\left(\frac{v_2}{v_1} - 1\right) + f\,\frac{A}{A_c}\frac{v_m}{v_1} - (1 - \sigma^2 - K_c)\frac{v_2}{v_1}\right] \tag{2.14}$$

Entrance effect Momentum effect Friction Exit effect

Frequently, the dominating term is the frictional term and all others can be neglected.

2.1.5 Effects of Axial/Longitudinal Conduction

All heat-exchangers are designed to create thermal gradients in both fluids. As a result, there will be conduction in the heat-exchanger structure, typically in the walls of tubes or plates, which will flatten the wall temperature distribution and reduce overall effectiveness. This is particularly true for single-pass exchangers with high effectiveness and short flow length. Kays and London explain that longitudinal conduction rate is given by [5]:

$$q_k \approx k\, A_k \frac{\partial t}{L} \tag{2.15}$$

Where A_k is the wall cross-sectional area for conduction, k is the material conductivity, L is the flow length, and ∂t is the temperature gradient in the wall. They suggest a decrement to effectiveness of the form:

$$\frac{\partial \varepsilon}{\varepsilon} \approx \frac{(k/L)\, A_k}{C_{min}} = \lambda \tag{2.16}$$

2.1.6 Plate-fin Heat Exchanger Geometry

A large number of heat-exchanger geometries exist for all flow arrangements. However emphasis will be placed on plate-fin geometry as this is the geometry selected for the SolarCAT recuperator.

Plate-fin geometry relies on extended surface (the fins) to supplement heat transfer area. Normally, the two flows are kept separate by the sandwich structure of the assembly. This approach permits the use of extended surface that is tailored to the needs of each fluid. Turbine exhaust is a low pressure, high temperature fluid. As a result, allowable pressure loss is typically very small to avoid the detrimental effects of back-pressure on the turbine. Low velocities are desirable the low-pressure side to keep pressure loss as small as possible. This can be achieved by increasing fin height (increasing free-flow area) and reducing fin blockage (lower fin density). However, both changes will also reduce effectiveness. Conversely, the compressor discharge flow is low-temperature, high-pressure air that can allow a much higher pressure loss and therefore internal extended surface will tend to be more restrictive (more fins per unit length) and have lower fin height. Some manufacturers accommodate the specific requirements of both compressor discharge and turbine exhaust sides by doubling the number of turbine exhaust layers in a unit-cell as shown in Figure 2-8. This technique halves the effective internal fin height and allows for twice as much frontal area for on the external side without additional plates. This figure also shows the manufacturing limit for ruffled fin at 43fpi (fins per inch) as both internal and external fins are folded to this manufacturing limit.

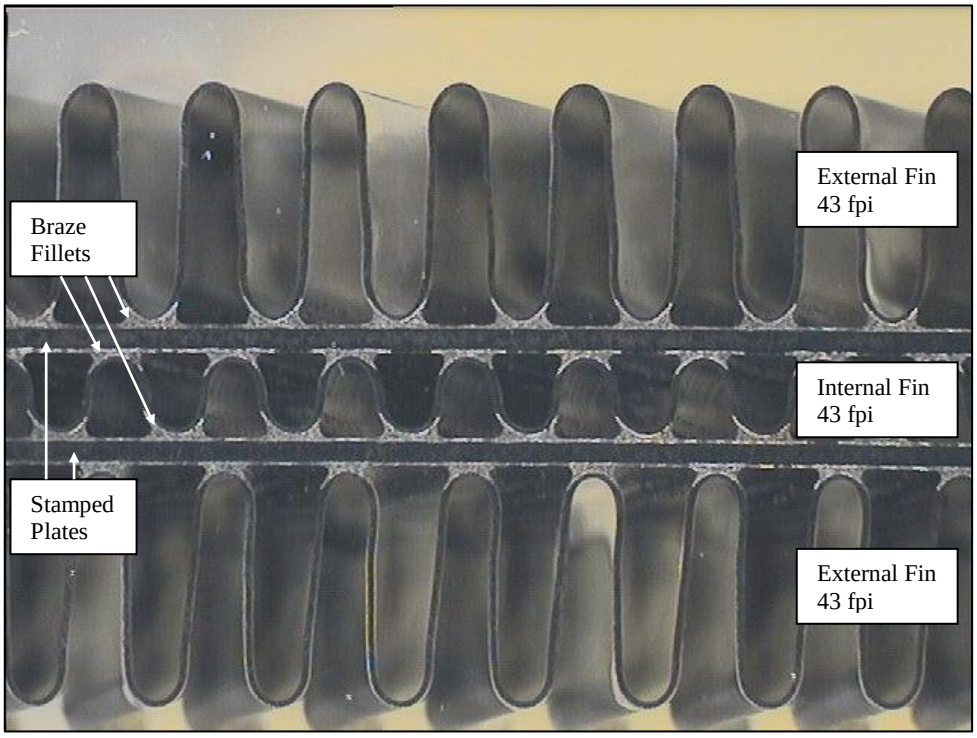

Figure 2-8 [Brayton Energy, LLC] Cut-section View of a Recuperator Unit-cell

2.2 Small Hydraulic Diameter Media Fabrication Techniques

2.2.1 Fin Folding

In this process, a coil of sheet metal is fed into a cyclic press where it is "folded" over a tool that varies in shape based on the desired fin profile. The figure below [Robinson Fin Machines, Inc.] illustrates some of the possibilities. Small hydraulic diameters can be achieved by minimizing fin height and maximizing fin density. A number of issues arise when fin height is exceptionally small. The cross-sectional profile no longer has a vertical segment normal to the stamped plates, which decreases the unit cell's burst pressure. Also, it becomes difficult to control the stamping process reliably when the desired draw height is very small, which in turn, makes the controlling brazing quality more difficult. A hydraulic

diameter of 0.68mm is the best that could be achieved with this technique using stainless steel and 0.076mm material.

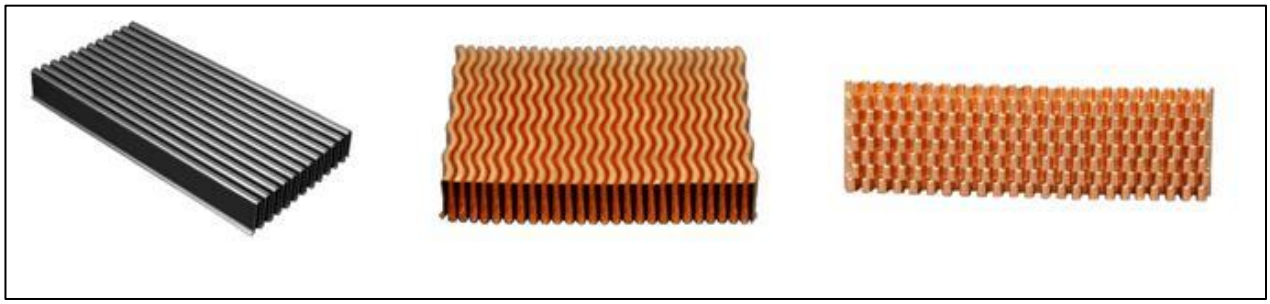

Figure 2-9 [Robinson Fin Machines, Inc.] Various Fin Types – Left to right: plain fin, ruffled fin, lanced fin

2.2.2 Packed Beds

A packed bed is a vessel that is filled with packing material that may take many forms. For comparison purposes, the packing material is assumed to be steel beads. Steel beads are a commodity item that can be obtained in many sizes and various alloys. These beads could be placed in the cavity between stamped plates and brazed or sintered, producing a periodic arrangement of beads and a well-defined geometry for analysis. In this manner, it is very simple to control the porosity of the medium by adjusting bead diameter. This process will behave as porous medium. Drawbacks include point-contact at all bead interfaces. The point-contact will become face-contact (small faces) with either sintering or brazing but the load path is indirect and the effective tensile section is relatively small. This disadvantage also applies to the conductive path normal to the stamped plates. Bead stacking will give generally isotropic physical properties.

2.2.3 Tubes

Using a technique similar to that described for packed beds, it would be possible to fill the cavity of the stamped plates with a large number of hypodermic needles (small diameter tubes) that could then be sintered or brazed to the plates. Again, these tubes are commodity items that are available with hydraulic diameters as small as 0.2mm (27gauge) in a variety of alloys, including stainless steels. The point-contact is replaced by a line-contact for the tubes. Although the line-contact is certainly better, there are still questions about structural integrity and effective thermal conductivity with this approach.

2.2.4 Cellular Metal Sandwich Structures

Figure 2-10 [6] shows a number of very interesting structural sandwiches. Structures (a) and (b) are Lattice Frame Materials (LFM's) made by forming perforated sheets. 3D Kagome structures (c) are made through investment casting. Structures (d) and (e) are woven textiles and (f) is a honeycomb structure that is not appropriate as it is closed-cell.

The LFM fabrication process is inefficient due to material scrape rate (very high) and long processing time (forming). Investment casting 3D Kagomes with very small hydraulic diameters (<0.7mm) is not easily achievable or cost-effective in a high-volume environment.

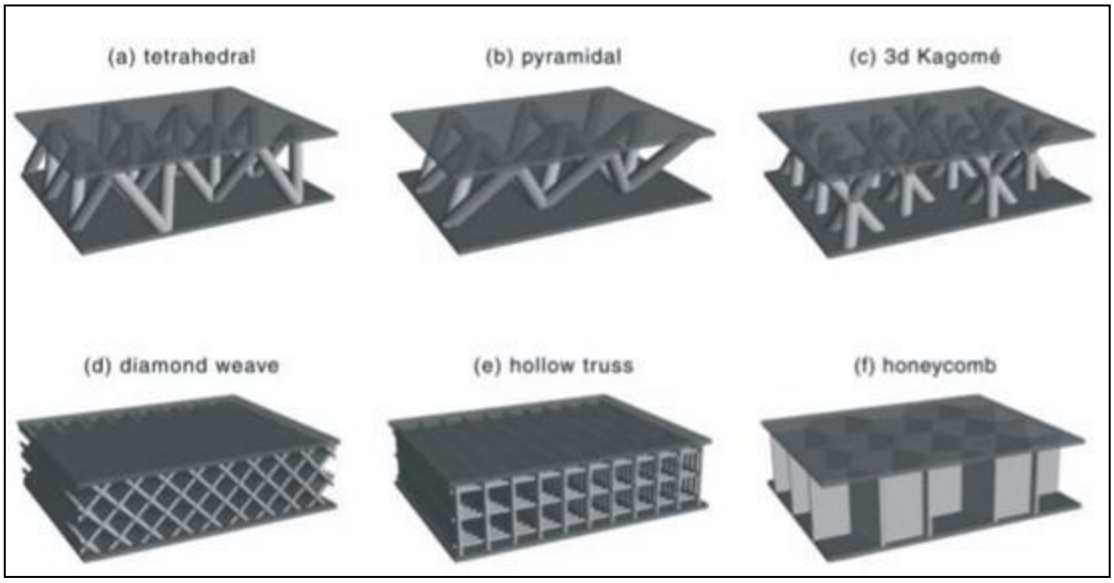

Figure 2-10 [6] Various Types of Periodic Cellular Metal Structures

The textile-based sandwiches have many advantages. Woven screen is a commodity item available in almost any alloy. It is possible to tailor the mesh density (mesh number or wires per inch) to each individual application. Stainless steel screen is readily available in 635# (635 wires per inch) with a hydraulic diameter of 0.015mm. Thermal conductivity normal to the plates should be good as there are direct conduction paths. The same is true for loading due to internal pressure as there are many wires contacting both plates. The textile-based extended surface is orthotropic in nature with significant properties normal to the flow direction and weaker properties in the direction of flow. Axial conduction concerns are minimized as there is little cross-sectional area in the longitudinal direction due point-contacts between adjacent wires.

2.2.5 Metal Foams

Metal foams have many qualities that would make them an excellent choice for compact heat exchangers. K. Boomsma [7] mentions that, "The open-cell metal foam structure has the desirable qualities of a well-designed heat exchanger, i.e. a high specific solid–fluid interface surface area, good thermally conducting solid phase, and a tortuous coolant flow path to promote mixing." Two basic independent characteristics define a metal foam: cell size and density. The two terms are considered to be independent with the density controlling ligament diameters and hence the strength of the foam in both tension and compression as well as the effective thermal conductivity of the foam. Cell size (or pore size) affects β as well as frictional loss terms.

A wide variety of metal foams are currently available. These foams are relatively inexpensive, easy to cut/form, and it is possible to tailor pore size to the particular application. In mass production, there would be little material waste as the fabricators could produce parts with the desired final shape (almost no cutting required). The cellular structure of the foam is quite random (Figure 2-11) although certain mathematical models assume an idealized periodic cell structure to assess the performance.

The foam has isotropic physical properties and as a result, axial conduction losses for the foams are more significant than textiles with wires normal to the stamped plates but much better than tubes or other axial structures such as micro-channels. Effective thermal

conductivity is worse than the textiles as there is no direct conduction path between plates (random ligament orientation). Xu and Wirtz [8] indicate that commercially available metal foams have effective thermal conductivities in the range of 2% to 6% of the base metal value. However, the critical drawback is their lack of tensile strength.

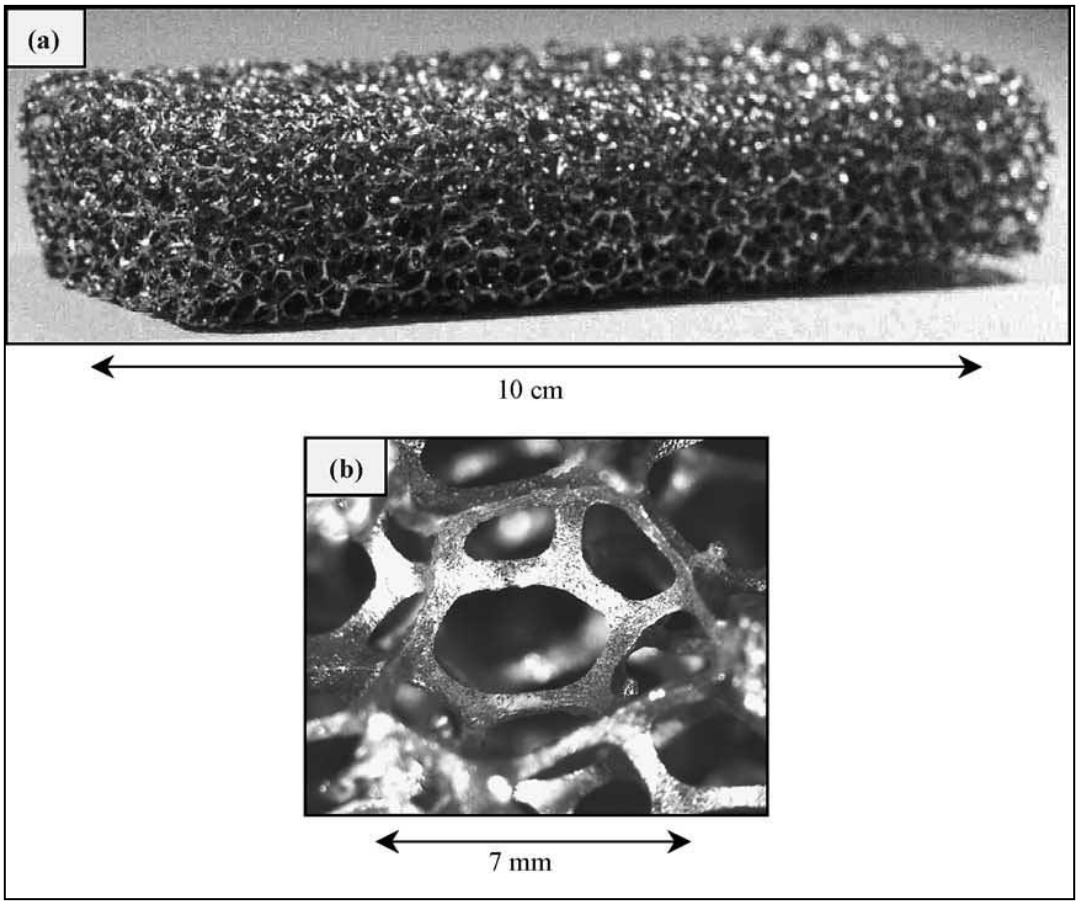

Figure 2-11 [7] Images of Aluminum Foam

2.2.6 Micro-channel

A heat-exchanger with features (channels) that are less than 1-2mm is often referred to as a micro-channel heat exchanger. The approach described in paragraph 2.2.3 (tubes) could also be considered micro-channel. This is a subject of intense research and a great deal of progress has been made recently. Although interesting, many of these techniques have not been fully commercialized and are cost-prohibitive or limited to research-scale projects.

Micro-machining covers a wide range of processes that include milling, grinding, sawing, etching, and many others. Any material can be used as long as it can be machined with the selected process. Channels are formed into a substrate by material removal. These channels can then be used as either primary or secondary surface for almost any heat-exchanger arrangement. The machined channels must then be assembled or bonded to avoid leakage of the contained fluids. Welding, brazing and diffusion bonding are some of the techniques used to bond the micro-machined plates together. Figure 2-12 shows a printed circuit etched plate made by Heatric, Ltd. The triangular regions on either side are turning headers with inlet and outlet at the top-left and bottom right. This plate is most likely a 7-pass cross-flow, overall counterflow arrangement. The wavy profile that has been chemically etched into the plate resembles that of a ruffled fin (see Figure 2-9). The plates immediately above and below the plate shown in Figure 2-12 would have flow passages etched in the longitudinal direction (top-to-bottom or bottom-to-top). The two types of plates are stacked sequentially to the desired overall height based on performance requirements. Once stacked, the plates are diffusion bonded and distribution manifolds are welded to the core.

Figure 2-12 [9] Typical Printed Circuit Heat-exchanger Plate (Heatric Ltd)

Stereo lithography is a process commonly used for rapid prototyping of plastics where a UV light causes a hardening of a thin layer of a reactive polymer to create a very thin solid layer. Successive passes allow the process to "build" almost any imaginable shape. While typically limited to features of about 0.125mm, it is possible to create very complex heat-exchanger geometry without expensive tooling or materials. The difficulty is that the process is limited to certain polymers. However, the polymer structure can be used to create a ceramic heat-exchanger through pyrolysis.

Another similar technique is Selective Laser Sintering (SLS) where a laser is used to selectively fuse powdered particles in a manner very similar to stereo lithography. Successive layers are fused to create a 3D form very quickly. This process is not limited to only polymers and can be used to form alloys such as titanium, steel and other alloys. Any geometry is conceivable but features are currently limited to about 0.25mm and removal of unfused powder can sometimes be difficult.

2.3 Flow Testing of Porous Media

2.3.1 Background

A great deal of work has been done over the past half-century to establish the performance characteristic of screens used in applications such as filters, wicks in heat-pipes, refrigeration, regenerators, combustion, and many others. In 1968, Armour and Cannon [10] used a packed bed model to obtain a general correlation predicting pressure drops across a diverse range of screen types through geometry-based variables including: surface area to unit volume ratio, void fraction and pore diameter. This study was limited to a single layer of screen and not applicable to laminate structures. Kays and London (1964) [5] also presented data for single layer woven-screen matrices with varying porosity.

2.3.2 Pressure Loss Studies

Heat-exchanger performance can be divided into two categories: pressure-loss and heat-transfer. The former is generally defined by a friction factor that is a combination of viscous

shear and form drag [5], permitting a comparison of any type of surface. Many authors have recently proposed correlations for different weaves, orientations and arrangements of screen. A few of the most pertinent will be discussed.

2.3.3 Sodré and Parise (1997)

Sodré and Parise [11] felt that little work had been done to establish a universal correlation that would be valid for any screen configuration. Prior studies were limited to a specific range of geometries and neglected edge effects. They used a modified form of the Ergun expression to develop an equation for friction factor including wall effects. They compared their correlations to work done by Armour and Cannnon [10], Kays and London [5], and Thonger and Rice (1986). The test sample was an annular arrangement of plain-weave #10 mesh screen with 165 layers (Figure 2-13). This arrangement was selected to mimic the radius ratios of the Stirling engine project they were working on at the time.

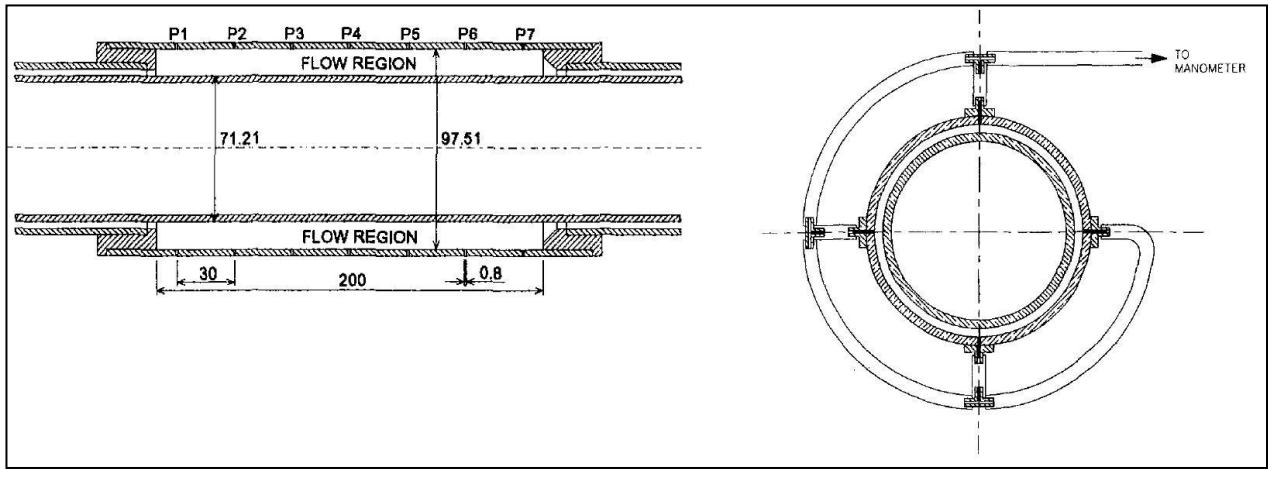

Figure 2-13 [11] View of Sodré and Parise Test Section and Pressure Taps

The air circuit they selected is complete and well thought-out as shown in Figure 2-14. They propose an equation stemming from the least squares method:

$$\frac{\Delta P}{L} = 100(1-\bar{\varepsilon})^2 \frac{\mu\, \bar{v} M^2}{[\bar{\varepsilon}^3 d^2]} + 0.73(1-\bar{\varepsilon}) \frac{\rho \bar{v}^2 M}{[\bar{\varepsilon}^3 d]} \tag{2.17}$$

Where $\bar{\varepsilon}$ is the average porosity, $\bar{v}$ is the average flow velocity, M is the Mehta and Hawley parameter (function of wire diameter, hydraulic diameter and porosity) [12], and d is the wire diameter. Their results aligned well with data from the authors mentioned above and equation x.x(above) is valid for fully developed turbulent flow of air at steady-state for a range of modified Reynolds ($M(1-\bar{\varepsilon})/Re$) from $1\ x\ 10^{-4}$ to 1 and mesh sizes from 10 to 200 mesh.

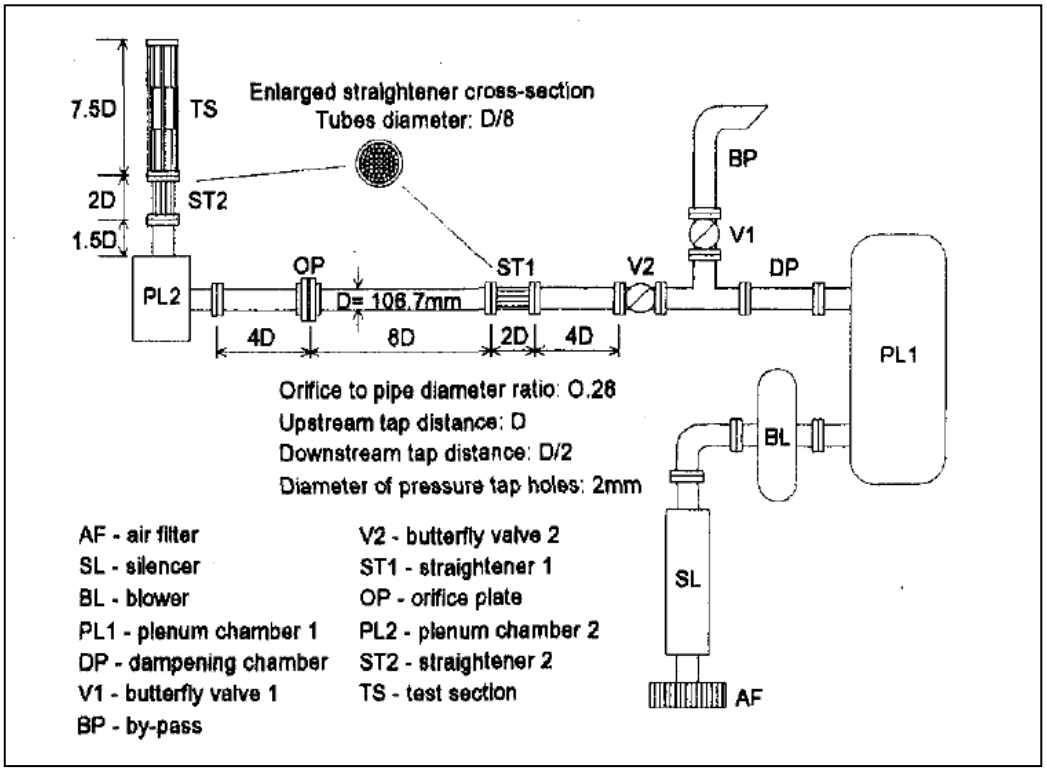

Figure 2-14 [11] Schematic of Sodré and Parise Air Circuit

2.3.4 Wu et al. (2005)

Wu et al. [13] build on the work of Sodré and Parise to determine if there is a general empirical equation suitable for many different weaves. They studied four types of screen weaves: plain, twill, fourdrinier, and dutch (Figure 2-15). They concluded that an empirical equation would be required for each weave type in order to accurately represent measured data.

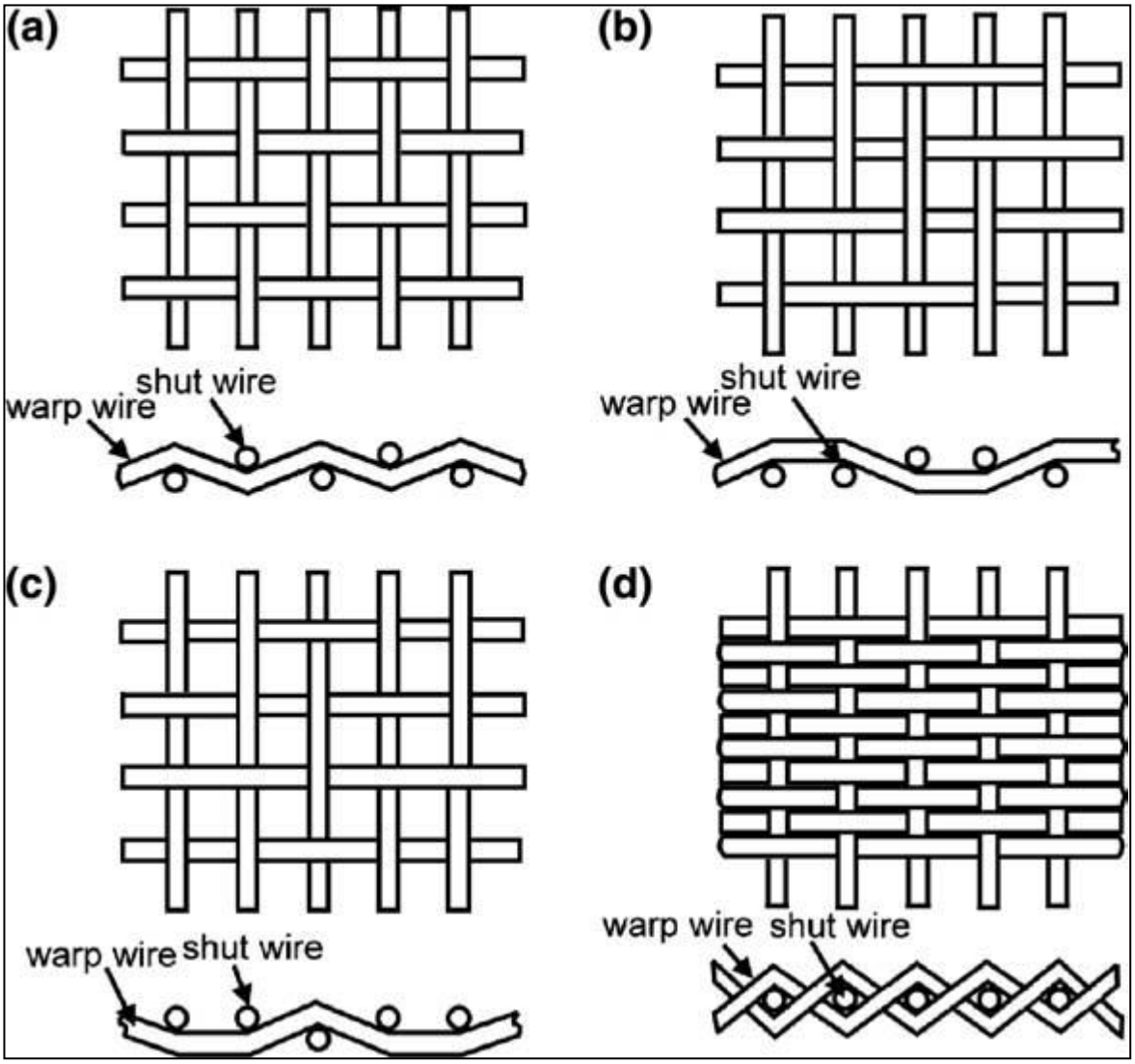

Figure 2-15 [13] Illustrations of Various Weaves : (a) plain; (b) twill; (c) fourdrinier; (d) dutch.

The air circuit they have chosen is clearly a derivative of the Sodré and Parise experiment (see Figure 2-16), although slightly simplified. The test section is 65mm in diameter and 200mm in length. There is no mention of brazing, bonding, or compression of the samples, so it is assumed that the test samples are loosely packed to fill the full 200mm test section.

They propose a modified Fanning friction factor equation based on a modified Reynolds:

$$\frac{Re}{(1-\varepsilon)} = \frac{D_P \rho U}{\mu} \tag{2.18}$$

$$D_P = \frac{6}{S_v} \tag{2.19}$$

$$f_k = \alpha \frac{(1-\varepsilon)}{Re} + \beta \left(\frac{1-\varepsilon}{Re}\right)^{\gamma} \tag{2.20}$$

Where D_P is the equivalent spherical diameter of the porous medium, S_v is the surface area per unit volume of solid phase, U is the fluid velocity, f_k is the friction factor, ε is the porosity, and α, β, γ are experimentally determined coefficients. They claim that the flow developing region is very short (about the length of one layer of mesh). The equation is valid for fully developed flow for porosities from 0.60 to 0.92 and modified Reynolds from 85 to 12000.

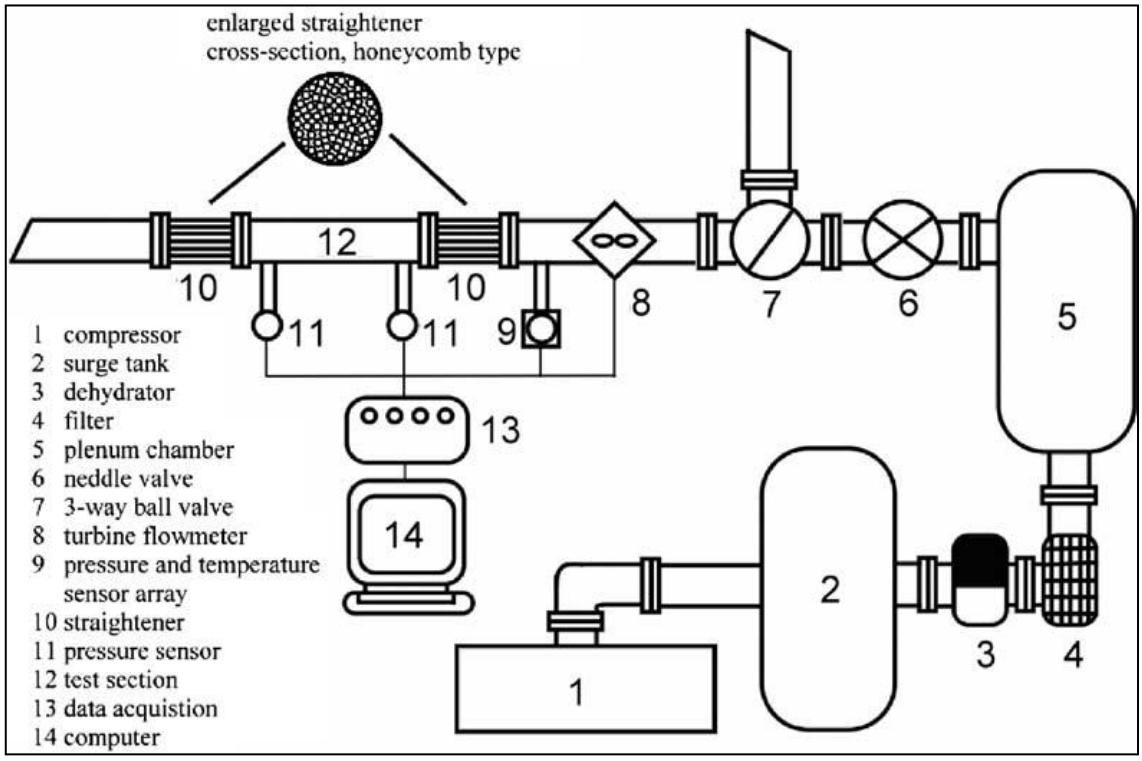

Figure 2-16 [13] Schematic of Wu et al. Air Circuit

2.3.5 Tian et al. (2004)

Tian et al. studied "The effects of topology upon fluid-flow and heat-transfer within cellular copper structures," [6]. They obtain data for both the pressure drop and Nusselt number (heat-transfer) for brazed textile-based structures and compare these results with the performance of several other heat-transfer media.

Their air circuit (Figure 2-17) is significantly different from either Sodré and Parise or Wu et al. in that Tian et al. have selected an open circuit suction-type system. They attempt to ensure fully developed flow entering the test section by using an inlet with a 4:1 contraction, a honeycomb flow straightener, and a long upstream channel with a length to channel height

ratio of 35. Both static and stagnation pressure taps were used to determine the upstream velocity profiles as shown in Figure 2-18. The rig is also designed for heat transfer measurements. One side of the test section was insulated while a heating pad was placed on the other side with a copper spreader plate to ensure even temperature distribution.

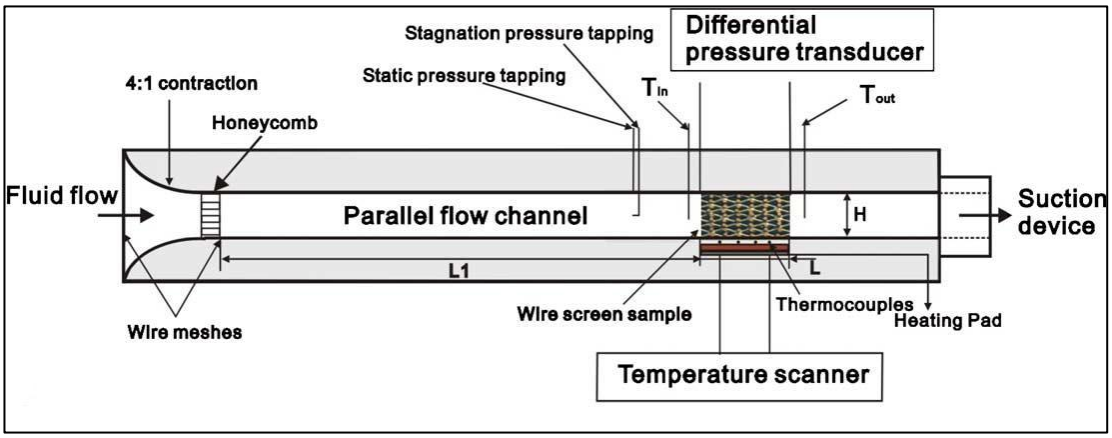

Figure 2-17 [6] Tian et al. Test Apparatus

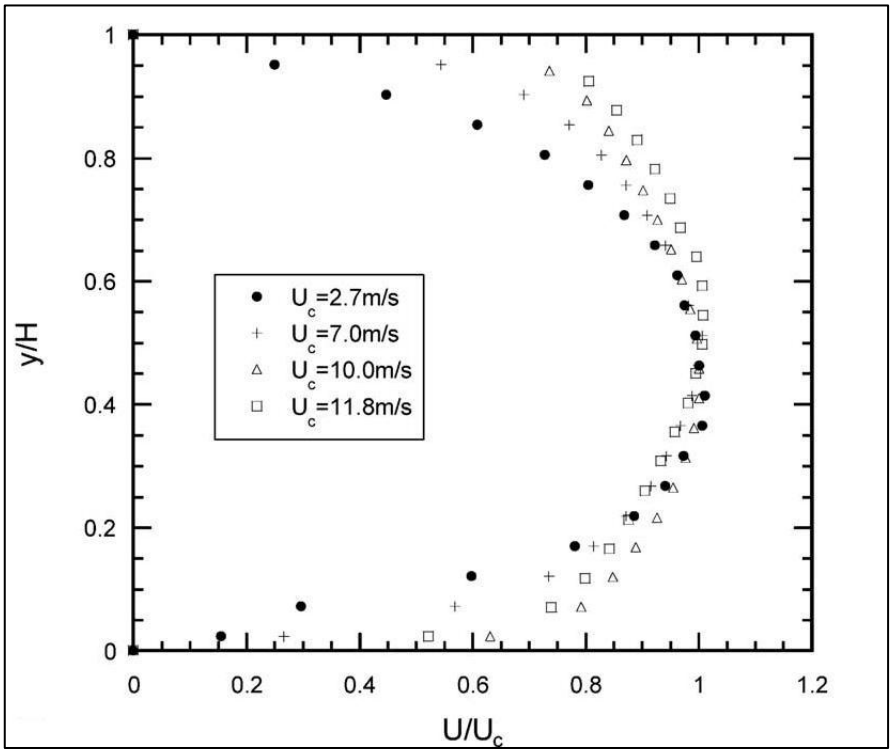

Figure 2-18 [6] Velocity Profiles from Tian et al. Study

Tian et al. suggest that because the screens are anisotropic, flow will behave differently along different orientations (front or edge – see Figure 2-19) and that a parameter other than porosity is required. They suggest:

$$R_{open} = \frac{Open\ area}{Total\ area} \tag{2.21}$$

Where open area is the unrestricted frontal area (free flow area) in the flow path and total area is the full frontal area in the flow path. They note that for equivalent samples, the friction factor for flow through the edge is approximately three times higher than for flow through the front of the sample. They propose a new definition of friction factor, K_{Cell} based on a unit length term, d_p:

$$K_{Cell} = \frac{\Delta P_{Cell}}{\rho\, U_m^2/2} = \left(\frac{\Delta P}{L} d_p\right)\left(\frac{1}{\rho\, U_m^2/2}\right) = \left(\frac{1 - R_{Open}}{R_{Open}}\right)^2 \tag{2.22}$$

Where $d_p = d + w$ for flow through the edge and $d_p = 2d$ for flow through the front.

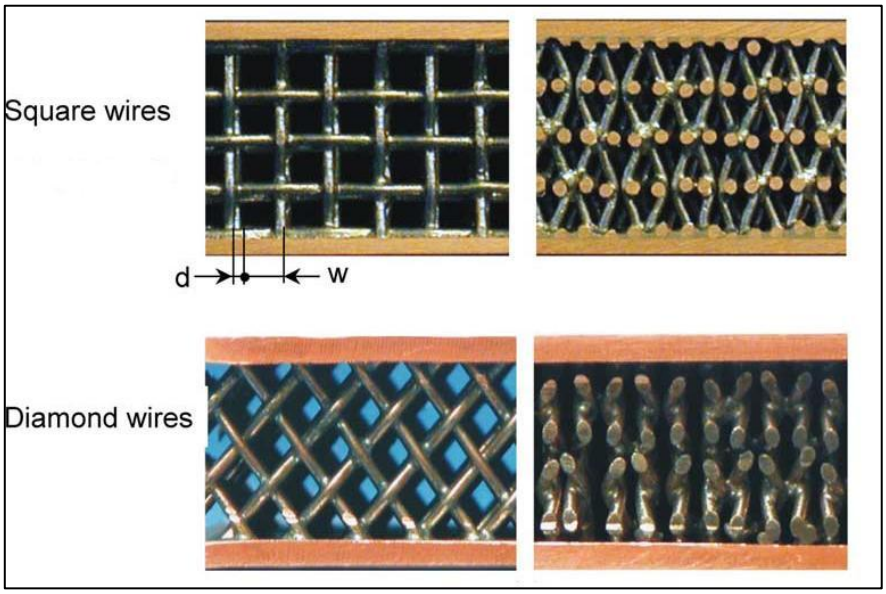

Figure 2-19 [6] Screen Orientations Used in Tian et al. Study (front on left, edge on right)

3. RESEARCH OBJECTIVES

3.1 General Objectives

The general purpose of this study is to assess replacement options for the internal folded fin of the SolarCAT recuperator. As previously indicated, the recuperator in question has an internal pressure loss budget of 2.0% but the current plate-fin design using folded fin as a high-pressure side extended surface cannot take advantage of the full budget due to manufacturing limitations. This situation indicates that the use of a smaller hydraulic diameter medium would be required in order to improve compactness of the heat-exchanger. The following figure, adapted from Kays and London [5], indicates the elements of heat-exchanger optimization in schematic form.

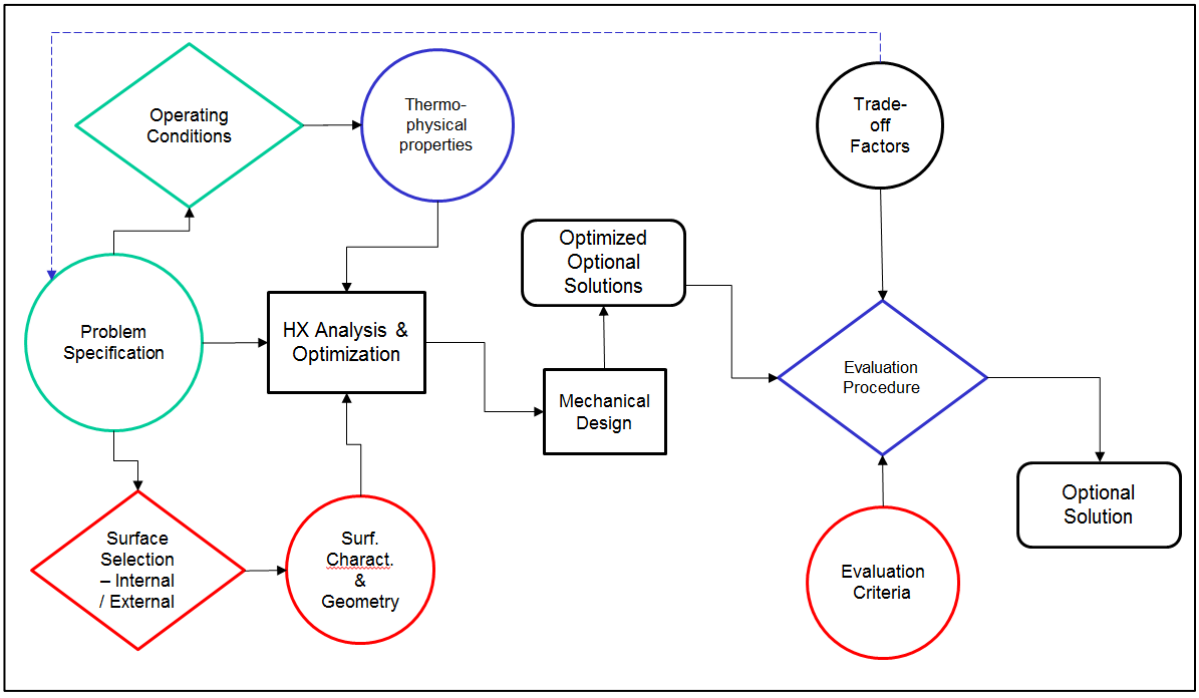

Figure 3-1 Heat-Exchanger Optimization Process

The items highlighted in green are those dictated by the project requirements. The thermo-physical properties of the fluids involved are dependent upon the temperatures which are defined by the project requirements. As a result, the only factors influencing the outcome are those related surface selection (highlighted in red).

3.2 Internal Medium Selection

A replacement medium must be selected for the folded fin. The chosen medium must satisfy the following criteria:

1. Hydraulic diameter smaller than 0.68mm.
2. May be manufactured as a wafer.
3. Must withstand an internal proof pressure of 3.9MPa.

In addition to the above criteria, the selection should consider fabrication elements affecting production costs such as material scrap in the process, availability of the raw material or components as well as performance considerations such as effective thermal conductivity, specific surface area and axial conduction losses.

3.3 Mathematical Representation of Selected Medium

Once a medium has been selected, its surface characteristics, as well as pressure loss and heat transfer characteristics must be represented as mathematical equations for integration into a heat-exchanger analysis program. Ideally, the mathematical representation should be a function of basic geometrical variables that fully define the geometry of the selected medium.

3.4 Validation of Selected Medium

Confirmation that the carefully chosen medium satisfies the aforementioned selection criteria is required. The first criterion, hydraulic diameter, can be demonstrated through measurement, optically, or by evaluation of geometric characteristics. The second criterion is a subjective assessment of current manufacturing processes. The final criterion can be demonstrated through physical testing. During a burst test, sample wafers are exposed to increasing internal pressures until failure. Failure sites are observed to improve braze techniques until an adequate, repeatable solution is found.

3.5 Integration of Mathematical Representation

Brayton Energy, LLC uses a proprietary heat-exchanger performance program using the ε-NTU method. This program permits sizing optimization of the recuperator given the operating conditions and specific surface geometry (see Figure 3-1). A new module needs to be added to this performance program integrating the mathematical representation of the selected fin replacement medium. Once complete, it will be possible to assess the effects of the new medium on recuperator size and cost.

3.6 Mechanical Design Constraints

Given that the objective of this study is to identify a small hydraulic diameter medium capable of replacing the existing SolarCAT recuperator internal fin, it is important to identify the form of medium to be assessed. The geometry of the internal fin can be altered in many ways but there are design criteria that need to be respected:

1. Matrix width: 168mm – due to constraints of the stamped plates
2. Internal fin height: 0.9mm to 6.5mm – reasonable range of fin heights
3. Internal fin flow length: 100mm to 200mm – due to core thermal strain management
4. Maximum high-pressure-side pressure loss: 2.0% - thermo-fluid design value
5. Effectiveness: over 94% - thermo-fluid design value

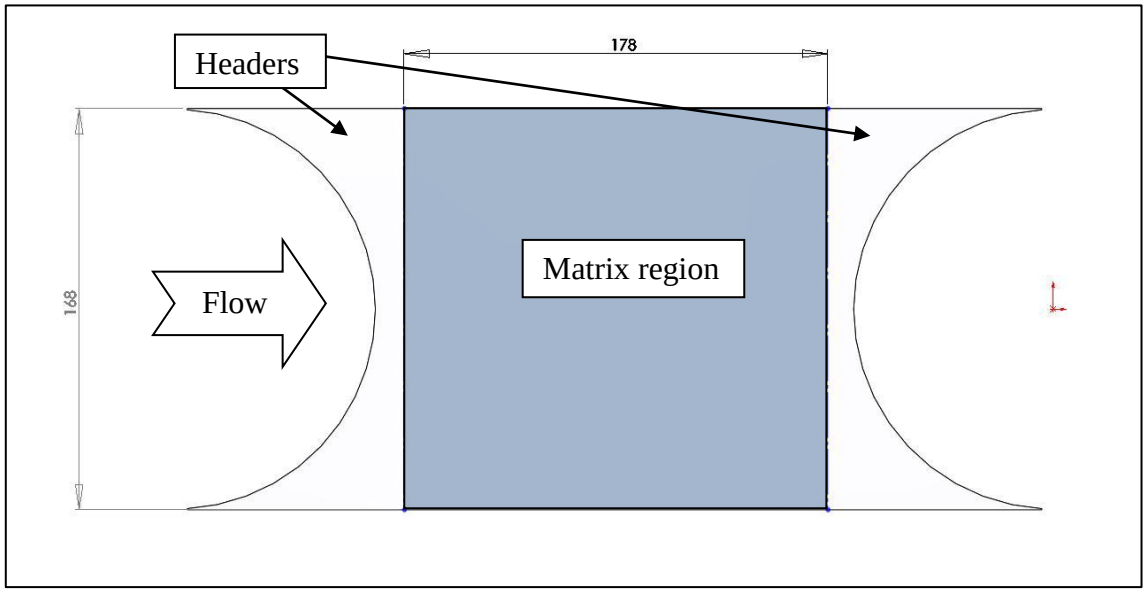

Figure 3-2 Internal Heat-transfer Extended Surface Geometry Limitations

4. INTERNAL MEDIUM SELECTION

4.1 Effect of Hydraulic Diameter

In most circumstances, there are significant benefits to improving the compactness of a heat-exchanger, as is the case for the SolarCAT recuperator. More so, there is pressure loss margin available in the current design. From the overall thermal resistance equation (Eqn. 2.2), it is clear that the convection terms for both fluids and the plate conduction term will affect the value of U. For reasonably conductive materials (most metals), it is often possible to neglect the conduction term as it is small in comparison with the convective resistance. From the definition of NTU, it is clear that in order to improve compactness, it is necessary to either increase U by improving the heat-transfer coefficient, increase heat-transfer surface area, or both. The definition of Nusselt:

$$Nu = \frac{h\, D_h}{k} \tag{3.1}$$

This equation demonstrates the dependence of h on D_h. Reducing the hydraulic diameter of a heat-transfer medium will increase h, and therefore increase effectiveness, but will also increase ΔP (Eqn. p.19).

Tian, et al. [6] compared the performance of several different heat-transfer media as a function of $\frac{Nu_H}{f^{1/3}}$ as shown in Figure 4-1. This study excludes the impact of longitudinal conduction losses which will be very important for highly compact micro-channel heat-exchangers with short flow lengths and large frontal areas.

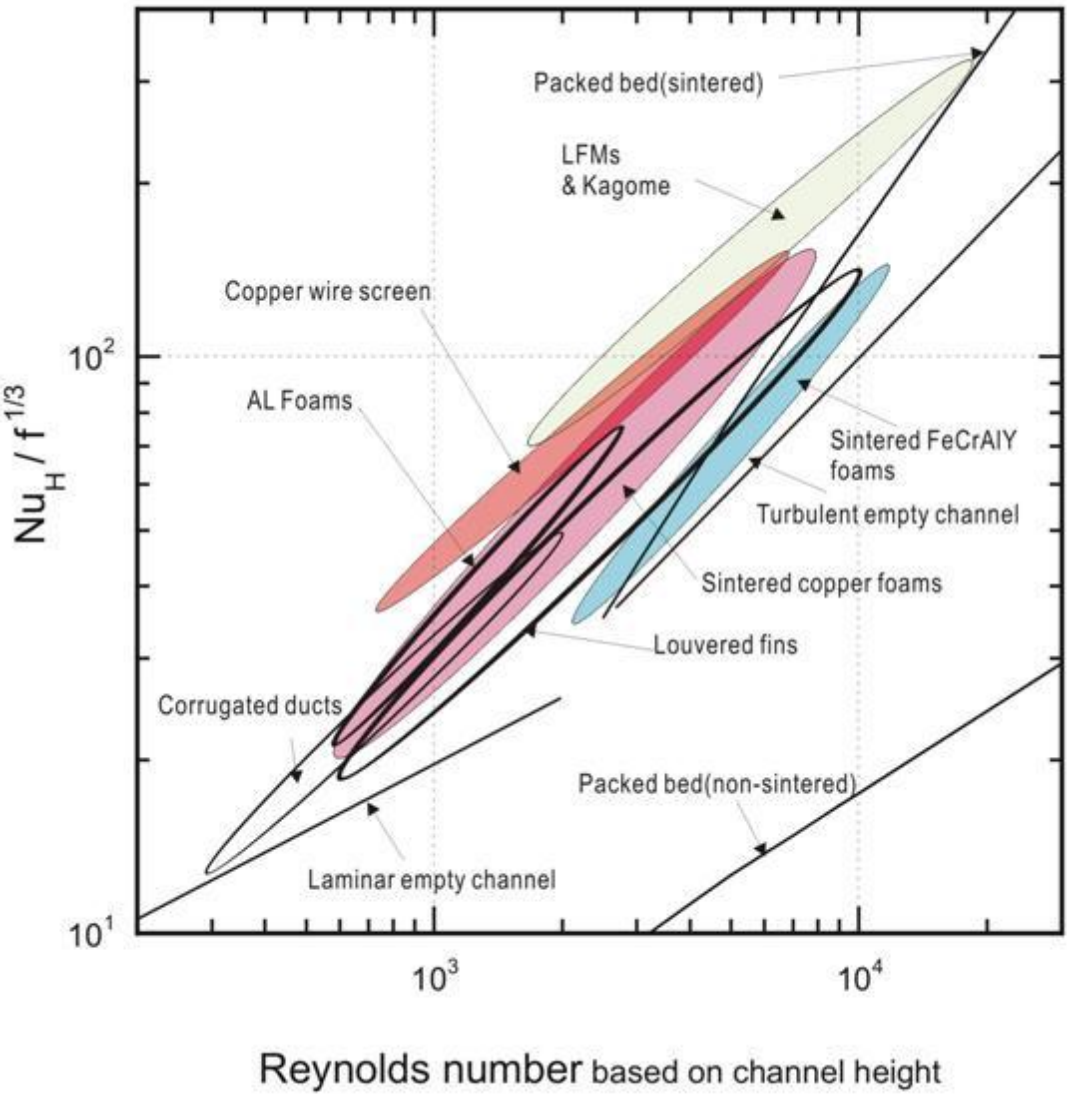

Figure 4-1 [6] Comparison of Various Heat-transfer Media

4.2 Packed Beds

The challenge with using a packed bed in this application is the requirement to create a wafer to replace the folded fin. In order to create the wafer, it would be necessary to form a sintered brick of steel spheres and slice it into wafers. As discussed in section 2.2.2, the quality of point-contacts between the spheres will limit both tensile strength and effective thermal conductivity. From basic geometry, it can be shown that:

$$D_h = \frac{\sqrt{12 - \pi}\,\emptyset}{\pi} \tag{3.2}$$

$$\beta = \frac{4\,\pi}{3\,\emptyset} \tag{3.3}$$

Where Ø is the sphere diameter. The smallest stainless steel ball bearing available was 0.5mm in diameter, which offers a hydraulic diameter, D_h, of 0.23mm and a specific surface area, β, of 8400m^{-1} in this configuration. The periodic structure of the packed bed creates a roughly isotropic material with effective thermal conduction normal to the flow direction being equal to the longitudinal component.

4.3 Micro-tubes

Both packed beds and micro-tubes are not used to their full potential in the proposed configuration and both suffer from similar complication given the need to create a wafer. Again a sintered brick would be fabricated containing a multitude of small diameter tubes. The brick would then be sliced into wafers to satisfy the design constraints. Neglecting tube wall thickness, it can be shown that:

$$D_h \cong \emptyset \tag{3.4}$$

$$\beta = \frac{2\,\pi}{\sqrt{3}\,\emptyset} \tag{3.5}$$

Where Ø is the tube diameter. The smallest readily available stainless steel tubes were 0.2mm in diameter, which offers a hydraulic diameter, D_h, of about 0.2mm and a specific surface area, β, of 18100m^{-1} in this configuration. The periodic structure of the stacked tubes creates a roughly orthotropic material with effective thermal conduction normal to the flow direction being significantly lower than the longitudinal component. The wafer configuration is clearly not well suited to this arrangement of tubes, which would likely be much more effective in a cross-flow arrangement with the tube walls separating high and low pressure fluids.

4.4 Cellular Metal Sandwich Structures

LFM's and Kagome's can be discarded (for now) due to the manufacturing difficulties involved in achieving hydraulic diameters smaller than 0.6mm in a cost-effective manner.

As mentioned in section 2.2.4, textile-based structural sandwiches have a number of distinct benefits. Like the packed bed spheres and micro-tubes, the textile must be held together through sintering to create wafers but the bond is created in the longitudinal direction where its weakness actually reduces conduction losses. The optimal conduction path is directed normal to the flow direction, which will benefit heat transfer and should provide excellent tensile strength. Screen-based wafers warrant further examination.

4.5 Metal Foams

Commercially available foams are typically found with pore sizes below 40PPI (pores per inch) which provides a hydraulic diameter of about 1.5mm and specific surface area of about $2200m^{-1}$. Metal foams are terribly weak in tension and will not withstand the internal pressure of the SolarCAT recuperator at operating temperatures as their tensile strength at room temperature is typically less than 2MPa.

4.6 Micro-channels

It is clear from equation 2.16 that most micro-channel heat-exchangers will suffer very significant performance decrements due to longitudinal conduction losses as hydraulic diameters approach the limits of the forming technique. When the channel dimension is close to the manufacturing tolerance limit, cross-sectional area for longitudinal conduction (A_k) is close to 50% of frontal area. Small channel size (small D_h) and high ratio of heat-transfer area to volume (β) will encourage large frontal area and short flow length (L) to minimize pressure loss for a desired target effectiveness. Both effects increase the decrement in effectiveness due to axial conduction. Many suppliers of such heat-exchangers suggest using lower conductivity materials to limit the impact of this effect even though reducing plate thermal conductivity will make the conductive resistance term more significant in the overall thermal resistance equation.

"Laminar and turbulent empty channels" from Figure 4-1 are effectively micro-channel heat-exchangers which will be discarded because of the previously mentioned losses. It should

also be mentioned that micro-machining techniques that achieve very small hydraulic diameters with large ratios of heat-transfer surface area to volume do so at the expense of a large fraction of the base material. In certain cases, mass of material removed can exceed the mass of the remaining material. As a general approach, it is the author's opinion that material addition is preferable to material removal through machining and material waste should be minimized with any given method.

4.7 Selection

Table 4-1 illustrates the properties of the aforementioned medium options in a manner that facilitates comparison. Items highlighted in red represent significant challenges to the adoption of this technique for production of wafers in this application. It is clear that there are real benefits to the use of textile sandwiches given the fantastic range of hydraulic diameters and specific surface areas and good effective thermal conductivity. As a result, this study will focus on the use of woven textiles for the SolarCAT application and will attempt select an appropriate mathematical representation to simulate the performance of the textiles, characterize various meshes, and assess real-world feasibility through proof-testing (burst testing).

Table 4-1 Summary of Small Hydraulic Diameter Fabrication Methods

Process	Dh [mm]	β [1/m]	K_{eff} [%]	σ_t	$\partial\varepsilon/\varepsilon$	Wafer? [Y/N]	Comments
Fin folding – wavy fin	> 0.68	<3070	*	HIGH	HIGH	Y	Large Dh requires long flow path
Packed Beds	> 0.2	< 8k	10-15	LOW	MED	N*	Steel beads – commodity Isotropic conductivity EDM wafers – expensive
Micro-tubes	> 0.2	< 18k	10-15	MED	HIGH	N*	Steel tubes– commodity Orthotropic conductivity – poor EDM wafers – expensive
LFM – lattice frame materials	> 0.6	TOO SMALL	Wide range	HIGH	LOW	Y	High material scrap rate Lengthy processing
3D Kagome	> 0.6	TOO SMALL	Wide range	HIGH	LOW	Y	High tooling costs – investment casting Dh generally quite large
Wire mesh (iso)	> 0.02	< 113k	< 23	HIGH	LOW	Y	Steel mesh – commodity Orthotropic conductivity – good Multi-wire wafering – cheap
Metal foam	> 1 typical	< 2k typical	2-6	LOW <2MPa typical	MED	Y	Available in sheets Isotropic conductivity
Micro-channel	> 0.25	< 8k	*	HIGH	HIGH	Y*	Material removal or SLM Slow and expensive techniques

4.8 Screen Wafers

Figure 2-10, items (d) and (e) illustrates a woven screen medium between parallel plates. This arrangement is appropriate for the SolarCAT recuperator. Tian et al. [6] indicate that the samples they constructed had a width of 40mm, height of 10mm and length of 60mm. However, the hydraulic diameters tested varied from 1.3mm to 2.8mm. The samples were constructed by means of a three-part braze process where individual screen sheets were brazed to bond the nodes and create a more rigid structure. These bonded screen sheets were then aligned, laminated and brazed. The final process brazed the laminate to face sheets, creating a textile sandwich.

The wafers created for this study were done in a similar manner. Layers of wire mesh were stacked and sintered into a brick (Figure 4-2) that is roughly a 100mm cube. The height of this brick (number of layers) defines the flow length of the wafers. The sintering process applies a load to the stack at temperature (proprietary values) and as a result there is always a significant amount of compression (cf<1). Low values for compression factor increase the specific surface area term and effective thermal conductivity. The sintered brick shown in Figure 4-2 has a compression factor of 65%. The screen brick was made square (Figure 4-3) and then was then cut into wafers with cuts normal to the least restrictive surface using wire EDM (Electric Discharge Machining) as shown in Figure 4-4.

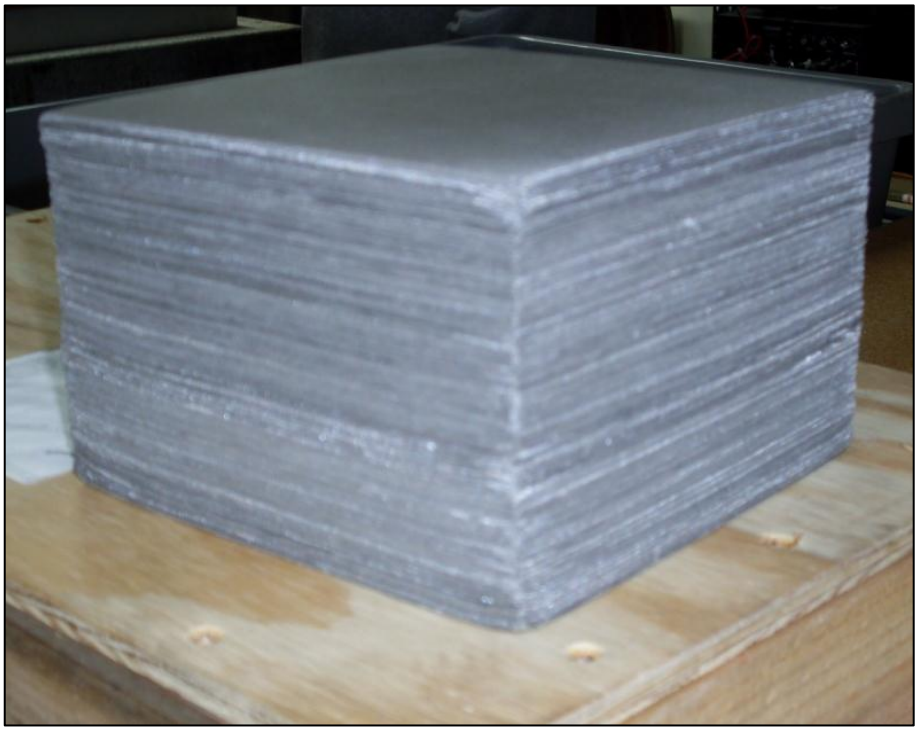

Figure 4-2 Sintered Screen Brick

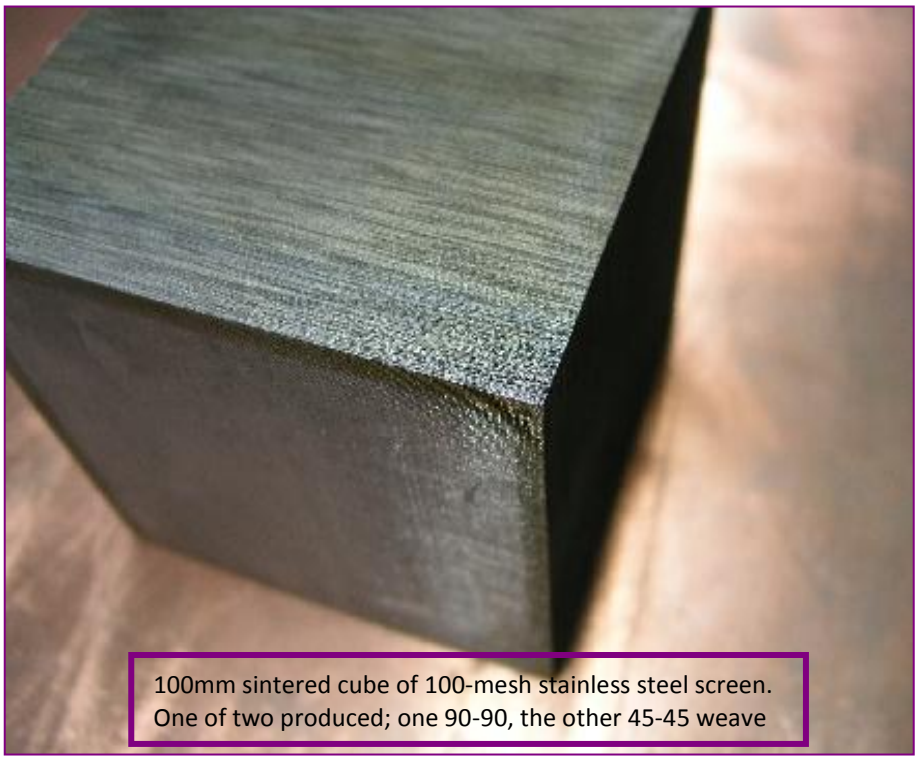

Figure 4-3 100mm Sintered #100 Mesh Cube

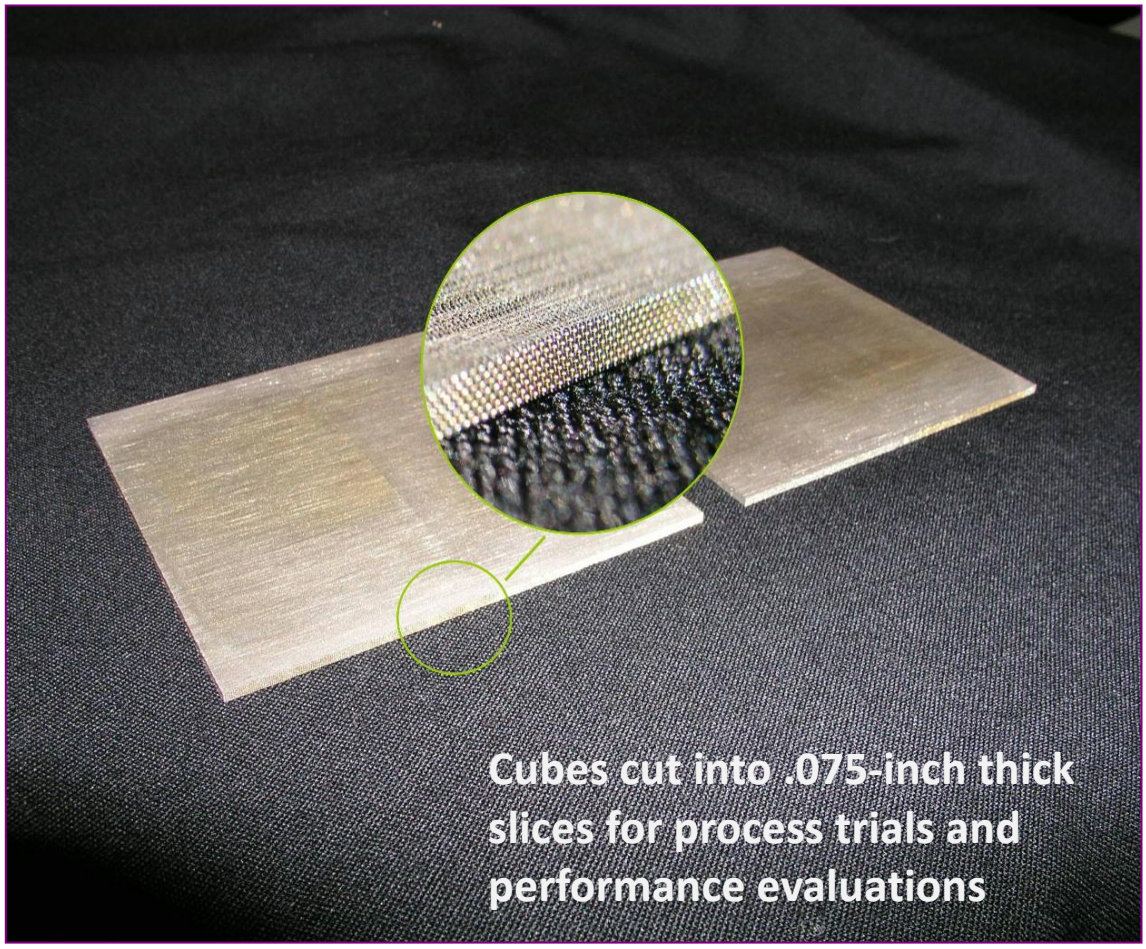

Figure 4-4 #100 Mesh Screen Wafers

5. MATHEMATICAL REPRESENTATION

5.1 Essential Equations

Calculating pressure loss for a given mesh is adequate for many applications. However, the design of a heat-exchanger requires more information. Accurately determining the heat-transfer characteristics of a medium is essential to the process. A few particularly pertinent articles will be discussed as they contain important mathematical descriptions of both geometric characteristics of screen as well as heat transfer elements required for the process.

5.1.1 Xu and Wirtz (2002) – Plain-weave Effective Thermal Conductivity

Xu and Wirtz [8] thoroughly describe a procedure to calculate in-plane effective thermal conductivity of plain-weave screen laminates. The concept of effective thermal conductivity is critical when evaluating potential high β (ration of heat-transfer surface area to volume) heat-exchange media. High β will increase the heat-transfer area but other characteristics such as ε (porosity) and tortuosity (twisting of flow path) impact the performance of a medium. This article provides an excellent mathematical model for the determination of effective thermal conductivity for a given plain-weave mesh from basic mesh geometry, material and fluid properties. They also discuss the concept of compression factor (cf), which accounts for nesting of adjacent layers of mesh in a laminate. A compression factor of 1 occurs when the shut wires from adjacent layers line up (Figure 5-1). When adjacent layers nest through compression or settling, the compression factor is said to be less than 1.

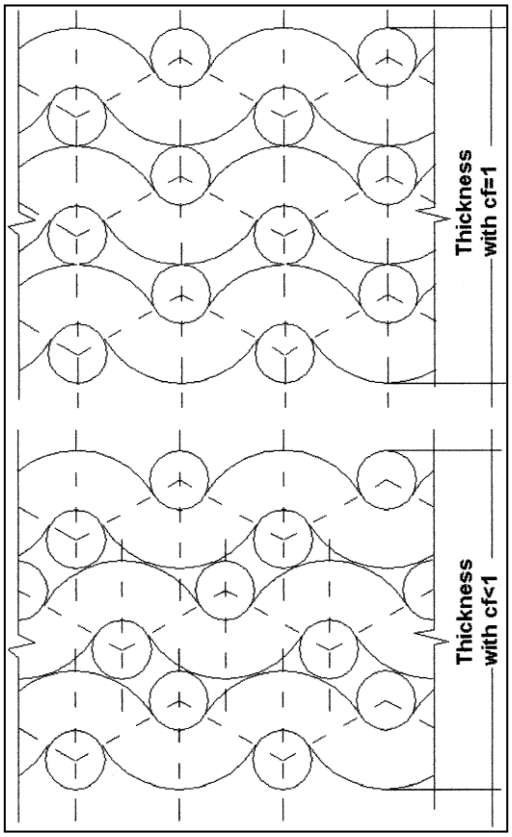

Figure 5-1 [8] Xu and Wirtz Illustrate Compression Factor

Xu and Wirtz define a number of basic geometric variables that are necessary for the calculation of effective thermal conductivity (Figure 5-2). Following is a summary of their nomenclature:

dx, dy	Diameters for the x and y direction filaments
$\bar{d}$	dx/dy
Mx, My	Mesh numbers along the x and y directions
$\bar{M}$	My/Mx
Sx, Sy	Wire filament lengths in unit cell
Mx^{-1}, My^{-1}	Wire filament pitch along the x and y directions

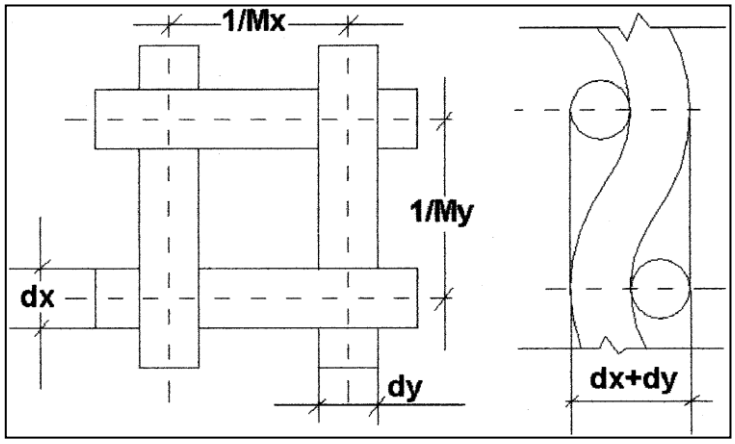

Figure 5-2 [8] Screen Geometric Variables

The wire filament lengths are given as follows:

$$Sx = \frac{1}{Mx}\left[1 + 9.6\left(\frac{dy\ Mx}{4}\right)^2 - 49.2\left(\frac{dy\ Mx}{4}\right)^4\right] \tag{5.1}$$

$$Sy = \frac{1}{My}\left[1 + 9.6\left(\frac{dx\ My}{4}\right)^2 - 49.2\left(\frac{dx\ My}{4}\right)^4\right] \tag{5.2}$$

When considering the impact of compression factor, the metal fraction (1-ε), is expressed as the reduced metal fraction:

$$cf\ (1-\varepsilon) = \frac{(\pi\ dy^2\ Sy + \pi\ dx^2\ Sx)\ Mx\ My}{4(dx + dy)} \tag{5.3}$$

The specific surface area, β is a function of the shape factor, SF:

$$SF = \frac{4(dy\ Sy\ Mx + dx\ Sx\ My)}{dy^2\ Sy\ Mx + dx^2\ Sx\ My} \tag{5.4}$$

and:

$$\beta = SF\ (1 - \varepsilon) \tag{5.5}$$

The in-plane thermal conductivity in the y direction is derived using a thermal circuit analogy and after some manipulation gives:

$$cf\ K_{ey} = \frac{160\pi\ Mx\ dy\ (K_{fs} - 1) + C\ cf\ K_{fs}}{(\bar{d} + 1)D} + \frac{C\ cf^2\ \bar{d}\ K_{fs}}{(\bar{d} + 1)(160\pi\ \bar{d}\ \bar{M}\ cf\ Mx\ dy(1 - K_{fs}) + C\ cf)} \tag{5.6}$$

Where

$$C = 123(Mx\ dy)^4 - 384(Mx\ dy)^2 - 640 \tag{5.7}$$

$$D = 123(My\ dx)^4 - 384(My\ dx)^2 - 640 \tag{5.8}$$

$$K_{ey} = k_{ey}/k_s \tag{5.9}$$

$$K_{fs} = k_s/k_s \tag{5.10}$$

k_{ey}	Effective thermal conductivity in the y direction
k_s	Thermal conductivity of the solid material
k_s	Thermal conductivity of the fluid

Equation 5.6 can be simplified for isotropic plain-weaves because the mesh number and wire diameter in both directions are identical.

Xu and Wirtz explain that screen laminates can be tailored for a wide range of porosity (ε), specific surface area (β), and effective thermal conductivity. These parameters will have a direct impact on the performance of the heat-exchanger. They also claim that isotropic plain-weave screen laminates can achieve effective thermal conductivity values as high as 23% and anisotropic variants can reach values as high as 78%. It is interesting to note that they indicate that metal foams are in the range of 2% to 6% and fused spherical beds are in the range of 10% to 15% effective thermal conductivity.

5.1.2 Park et al. (2002) – Heat Transfer Model

Park et al. [14] provide a mathematical model to assess the thermal-hydraulic performance of isotropic plain-weave screen laminate media. The experimental setup for pressure loss measurements is open-loop with induced draft. Compressed air passes through a flow straightener, the test article, another flow straightener, into a plenum, through a long pipe, a flow meter, and exits through a variable exhaust. A closed-loop water-flow rig is used for the heat-transfer measurements. The test article is 100mm wide by 18mm tall and only 4.32mm in flow length. They give an equation for mesh hydraulic diameter:

$$D_h = \frac{4\varepsilon}{\beta} \tag{5.11}$$

This article provides friction factor and Colburn modulus vs. Reynolds data over a useful range but the sample flow length is so small that the data is likely affected by entrance effects.

5.1.3 Xu and Wirtz (2002) – Weave Angle

Xu and Wirtz also discuss the effects of changing weave orientation and weave angle on isometric plain-weave screen laminate parameters ε, β, and k_{ey}. They find that changing only the orientation (Figure 5-3) of the mesh with respect to the direction of heat flux does not impact effective thermal conductivity, porosity or specific surface area. However, changing the angle (θ) between the woven wires (Figure 5-4) can have a significant impact on the performance parameters. There is a physical limitation to the minimum weave angle (2θ) of π/4 where the ratio of effective thermal conductivity of the diamond-shaped mesh over the effective thermal conductivity of the plain-weave is a maximum of 2.4.

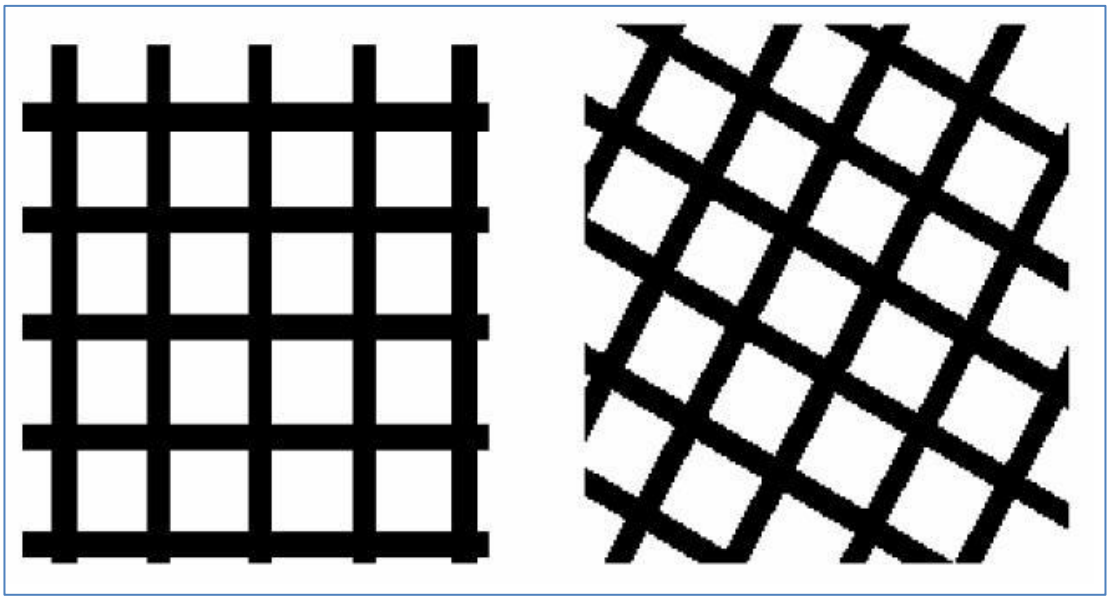

Figure 5-3 [15] Changing Weave Orientation

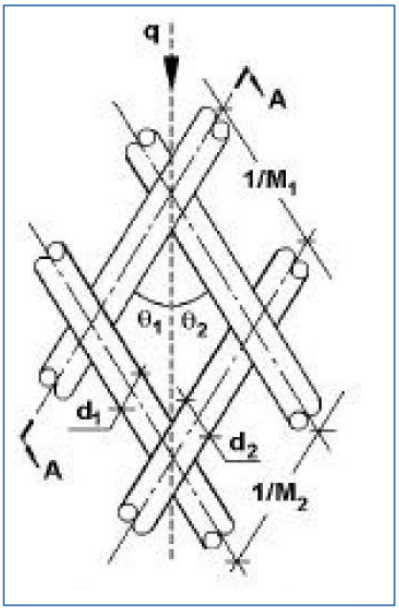

Figure 5-4 [15] Changing Weave Angle

5.1.4 Wirtz et al. (2002)

Wirtz et al. [16] examine the thermo-hydraulic performance of a 3D woven mesh structure for use as a heat-exchanger medium. This study extends from the work of Xu and Wirtz on in-plane effective thermal conductivity in 2002. The 3D weave (Figure 5-5) allows for a controllable anisotropic product where the thermal performance properties in each direction can be tailored to meet specific needs. The addition of a wire in the flow direction has the advantage of increasing the range of achievable values of β and adjusting wire diameters and mesh numbers in the direction of heat flux will allow for very high effective thermal conductivity. The article includes equations for effective thermal conductivity, friction factor, Colburn modulus and comparisons with test data. The authors mentioned that the weaving setup was lengthy and that it was difficult to maintain a tight mesh.

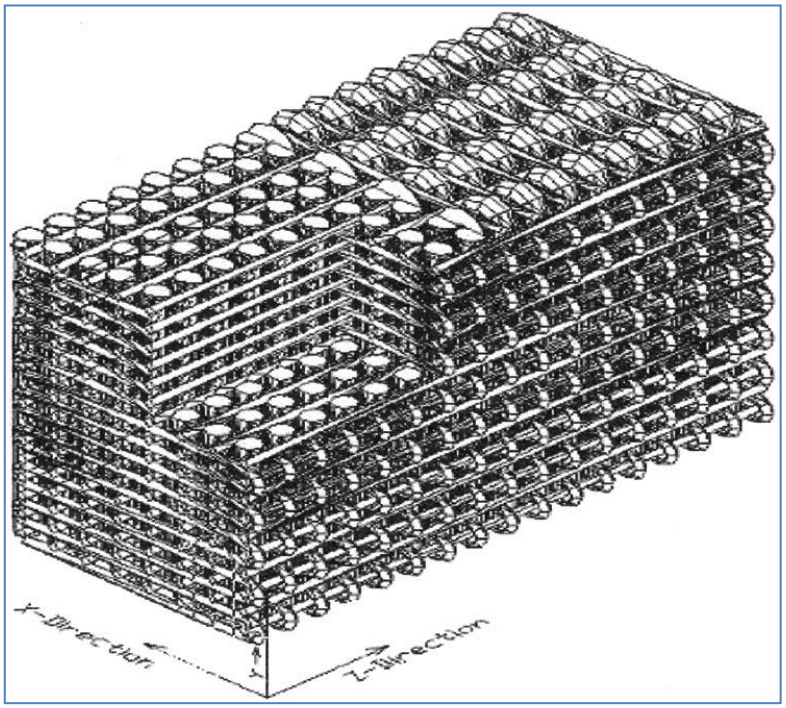

Figure 5-5 [16] 3D Woven Mesh

5.1.5 Li and Peterson (2006) – Effective Thermal Conductivity

Li and Peterson [17] study the impact of contact resistance on effective thermal conductivity of a single layer of screen and multi-layer laminates. They compare thirteen different models for effective thermal conductivity with results obtained from testing. They propose a mathematical model that can be drastically simplified when thermal conductivity of the solid is greater than 100 times that of the fluid. The simplified equation for non-dimensional thermal conductivity (isotropic plain-weave) is:

$$K_{ey} = 1.42\ (M\ d)^2/cf \tag{5.12}$$

They also propose a simplified equation porosity given a laminate consisting of isotropic plain-weave mesh:

$$\varepsilon = 1 - \frac{M\ d\ \sqrt{1 + (Md)^2}}{4\ cf} \tag{5.13}$$

Li and Peterson indicate that it is possible to achieve very high values of effective thermal conductivity but contact conditions are crucial in determining the magnitude of conductivity.

5.1.6 Vafai and Kim (1989 & 1995)

Vafai and Kim [18] discuss an exact solution for a channel filled with a porous medium. They demonstrate a solution for fully developed forced convection in a porous channel with parallel plates, assuming a homogenous, isotropic medium with no axial conduction effects. They define the Darcy number (Da) and inertia parameter (Λ_I) as a function of permeability (K) and Forchheimer coefficient (F) as follows:

$$Da = \frac{1}{H^2}\frac{K}{\delta} \tag{5.14}$$

$$\Lambda_I = \delta^{2/3}\ F\frac{u_\infty\ H}{\nu_f} \tag{5.15}$$

where

H	half-channel height
δ	porosity
u_∞	x component of velocity outside the momentum boundary layer
ν_f	kinematic viscosity

Vafai and Kim then proceed to demonstrate the mean velocity (u_m) for thermal boundary layer calculations, and temperature profile in the channel subjected to constant wall heat flux. From this, they provide two representations of the Nusselt number:

$$Nu = \frac{h\, D_h}{k_e} \tag{5.16}$$

$$Nu = \frac{4{u_m}^2}{\Gamma} \tag{5.17}$$

Where D_h is the hydraulic diameter, k_e is effective thermal conductivity, and Γ is a dimensionless parameter defined to simplify the equation. It should be noted that u is the dimensionless x component velocity ($u = \langle u \rangle / \mathrm{u}_\infty$) and that u_m is also dimensionless. The following equation for heat-transfer coefficient, h, results:

$$h = \frac{k_e}{D_h} \frac{4{u_m}^2}{\Gamma} \tag{5.18}$$

They conclude that for high-permeability media, both Darcy number and inertia parameter play a role in the thickness of the momentum boundary layer and have an effect on Nusselt number. Conversely, low-permeability media can neglect inertial effects (see Figure 5-6).

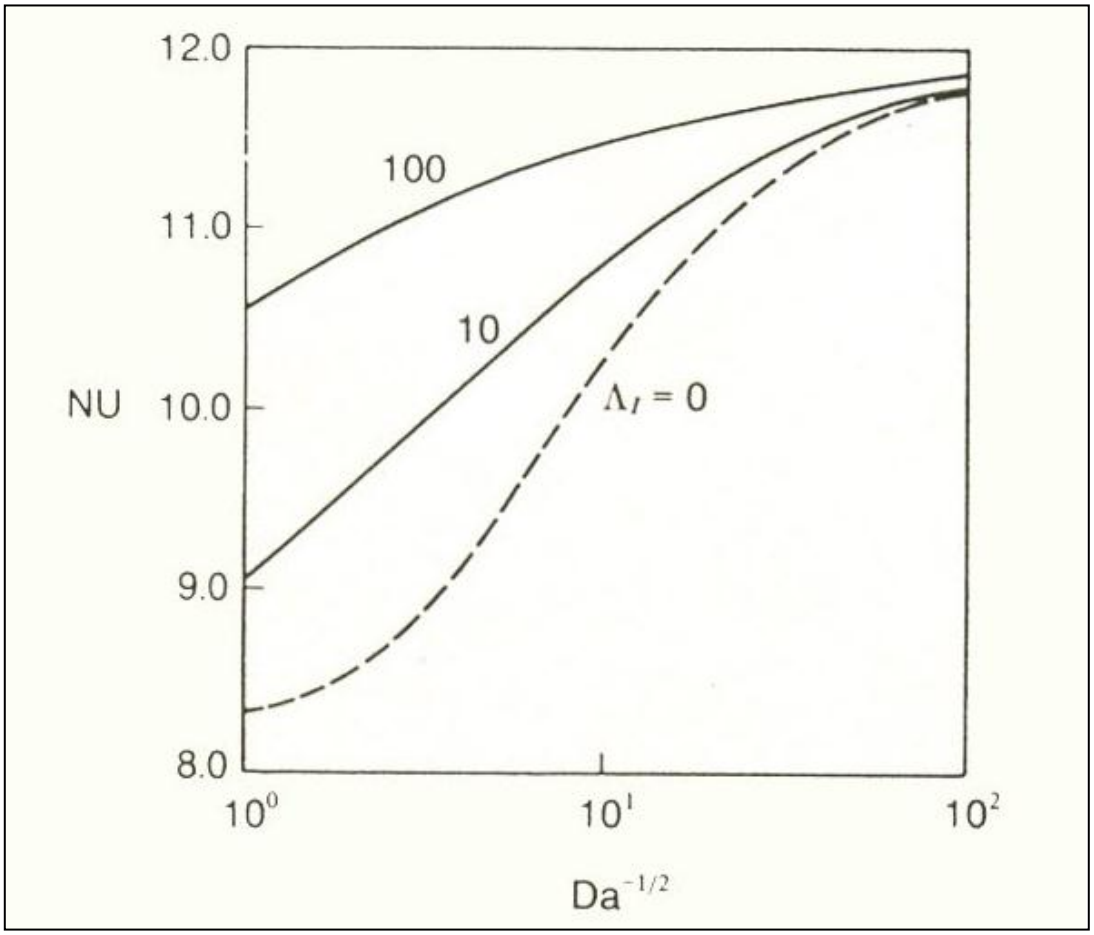

Figure 5-6 [18] Vafai and Kim (1989) Variation of the Nusselt Number

5.2 Integration

The model presented by Vafai and Kim [18] is ideal to simulate the proposed wafers with flow lengths up to 200mm and very small hydraulic diameters. The wafers are a porous medium between two parallel plates with fully developed forced convection within. Unlike the models proposed by Tian et al. [6], Xu and Wirtz [8] [15], Wirtz et al. [16] and Park et al. [14], where empirical relations for Nusselt number vs. Reynolds number or Colburn modulus vs. Reynolds number are proposed, Vafai and Kim express Nusselt number as a function of the Darcy number and the inertia parameter, which can be obtained experimentally through simple flow testing [19] or the use of a generalized equation such as the ones proposed by Wu et al [13].

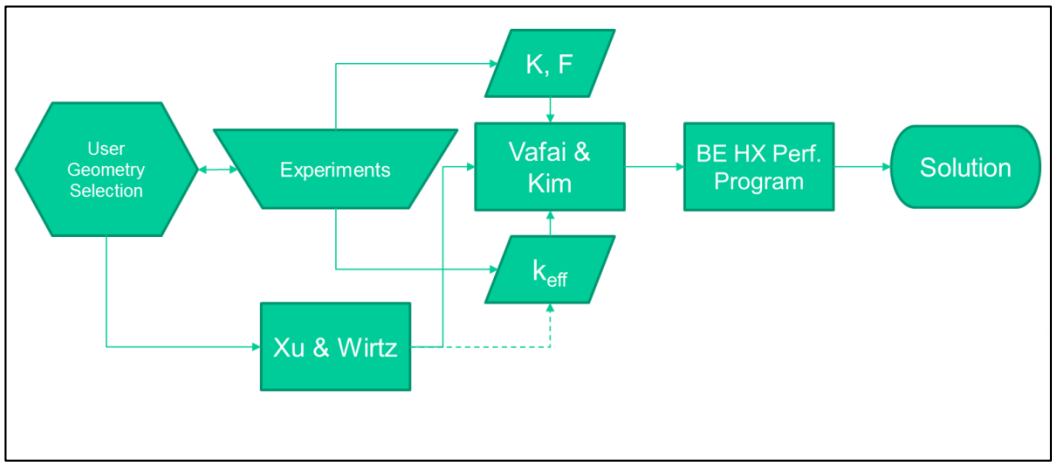

Figure 5-7 Schematic of Mathematical Representation - Experimental

Figure 5-7 illustrates the path to obtaining all the information required for the heat exchanger performance program. Experiments must be completed to acquire the data necessary to determine the permeability and Forchheimer terms for integration into the Vafai and Kim

model which will yield a heat transfer coefficient. The determination of effective thermal conductivity could be done either through experimentation of with the help of either the Xu and Wirtz model [8] or the Li and Peterson model [17]. It is assumed that all geometric equations could be expressed as shown by Xu and Wirtz [8]. This approach limits the user by forcing the selection of a screen configuration (mesh number and wire diameter) that has been tested and incorporated into the program. The ideal solution likely requires a screen configuration somewhere between those that have been tested.

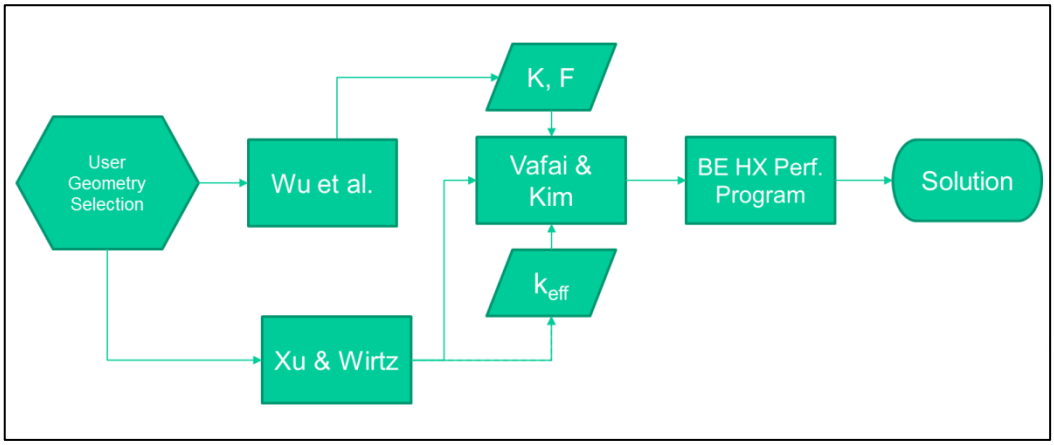

Figure 5-8 Schematic of Mathematical Representation - Equations

By using a generalized equation for pressure loss, it becomes possible to avoid testing every configuration of interest as shown in Figure 5-8.

Given the long flow path of the proposed heat-exchanger, a model for fully-developed forced convective flow must be used to assess the heat-transfer within the recuperator. The model discussed in chapter **Error! Reference source not found.** by Vafai and Kim [18] assumes

non-Darcy flow using the Darcy-Forchheimer flow equation to obtain the parameters necessary for the model. Antohe et al. [19] discuss methods to characterize porous media through experimental testing. They suggest quadratic interpolation using the least-squares method given the Darcy-Forchheimer equation:

$$\frac{\Delta P}{L} = \frac{\mu}{K} v_D + \frac{\rho\, c_F}{\sqrt{K}} {v_D}^2 \tag{5.19}$$

Where K is permeability, v_D is the Darcy velocity (superficial velocity) and c_F is the Forchheimer coefficient.

For isotropic plain-weaves for the available range of velocities Wu et al. shown that:

$$f_k = 250 \frac{1-\varepsilon}{Re} + 1.69 \left(\frac{1-\varepsilon}{Re}\right)^{0.071} \tag{5.20}$$

They also show that:

$$f_k = \frac{\Delta P}{L} \frac{D_P}{\rho U^2} \frac{\varepsilon^2}{1-\varepsilon} \tag{5.21}$$

And:

$$D_P = \frac{6}{S_v} \tag{5.22}$$

Rearranging (x) and (y):

$$\frac{\Delta P}{L} = \frac{1-\varepsilon}{\varepsilon^2} \left[250 \frac{\mu}{{D_P}^2} U + 1.69 \left(\frac{\mu}{D_P\, \rho\, U}\right)^{0.071} \frac{\rho}{D_P} U^2 \right] \tag{5.23}$$

Equation 5.23 presents the generalized Wu et al. equation (equation 5.20) in a form that simplifies the evaluation of permeability and Forchheimer coefficients using the Darcy-Forchheimer equation above. Isolating permeability:

$$K = 0.144 \frac{\varepsilon^2}{{S_v}^2 (1 - \varepsilon)} \tag{5.24}$$

And Forchheimer coefficient:

$$c_F = 0.094 \sqrt{\frac{(1 - \varepsilon)}{\varepsilon^2}} \left(\frac{\mu S_v}{\rho v_D}\right)^{0.071} \tag{5.25}$$

Where ε is porosity.

Inserting equation 5.24 into equation 5.14 yields the following equation for Darcy number:

$$Da = \frac{0.144}{H^2} \frac{\varepsilon}{{S_v}^2 (1 - \varepsilon)} \tag{5.26}$$

The inertial parameter is obtained by inserting equation 5.25 into equation 5.15:

$$\Lambda_I = 0.094 \, H \, {S_v}^{0.071} \sqrt{\frac{1 - \varepsilon}{\varepsilon}} \left(\frac{\rho v_D}{\mu}\right)^{0.929} \tag{5.27}$$

These parameters can now be used to solve for Γ and u_m as discussed in chapter 5.1.6. Using equation 5.18 to calculate the heat transfer coefficient within the porous medium, this mathematical model can easily be integrated into Brayton Energy's proprietary recuperator sizing program. The entire process is shown in Figure 5-9 below.

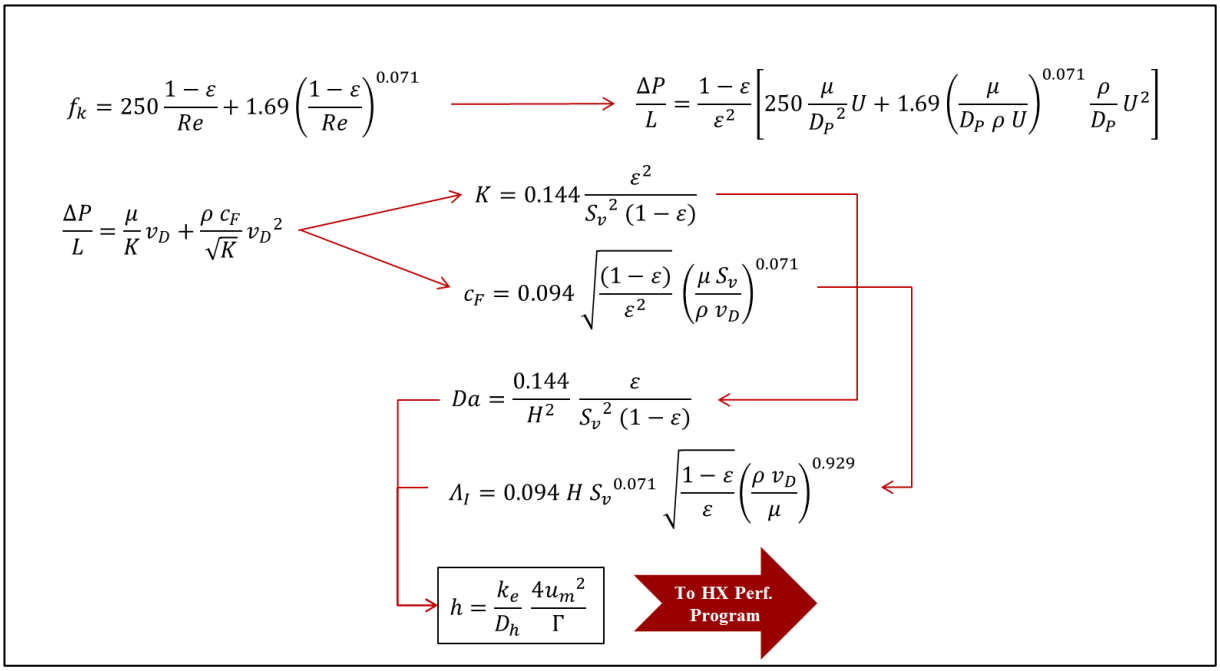

Figure 5-9 Flow of Data to the Performance Program

6. VALIDATION

6.1 Flow Test Objective

As discussed in section 5.2, it is preferable to incorporate a generalized equation for pressure loss through isotropic-weave screens into the performance program given that the generalized equation is valid for the screen configurations of interest. Flow testing will validate the use of these equations.

6.2 Flow Test Sample Selection

Four isotropic-weave configurations were selected for flow testing as well as two Dutch weaves. Initial testing was limited to isotropic plain-weaves meshes. The coarsest isotropic-weave tested has a hydraulic diameter equivalent than that of the 43fpi ruffled fin (see Table 6-1) but higher specific surface area. Porosity and specific surface area terms have been calculated assuming a compression factor of unity.

Table 6-1 Geometric Data for Flow Test Samples

Mesh #	Material	Wire Diameter [mm]	Hydraulic Diameter [mm]	ε, Porosity [%]	β, Specific Surface Area [m^2/m^3]
Ruffled fin 43fpi	304 Stainless	N/A	0.68	N/A	2750
30	304 Stainless	0.30	0.68	68	4330
60	304 Stainless	0.19	0.29	60	8270
80	304 Stainless	0.14	0.21	62	10970
100	304 Stainless	0.11	0.18	60	13770

6.3 Flow Test Apparatus

The objective for the design of this flow test rig was to simplify the setup as much as possible based on the results of authors performing similar studies. The air circuit for this flow test apparatus is shown in Figure 6-1 and is based largely on the air circuit used by Wu et al (Figure 2-16). No flow straighteners were added to the system as the 10D section upstream of the test article was deemed adequate. Portable data acquisition units were used to take pressure and temperature measurements throughout testing (see Figure 6-2). A hot-wire anemometer was used to confirm velocity measurements calculated from rotameter readings. Pressure taps were positioned as shown in Figure 6-3 and a close-up of the test section is shown in Figure 6-4. The test section inner diameter is 63.5mm and flow length is 75mm.

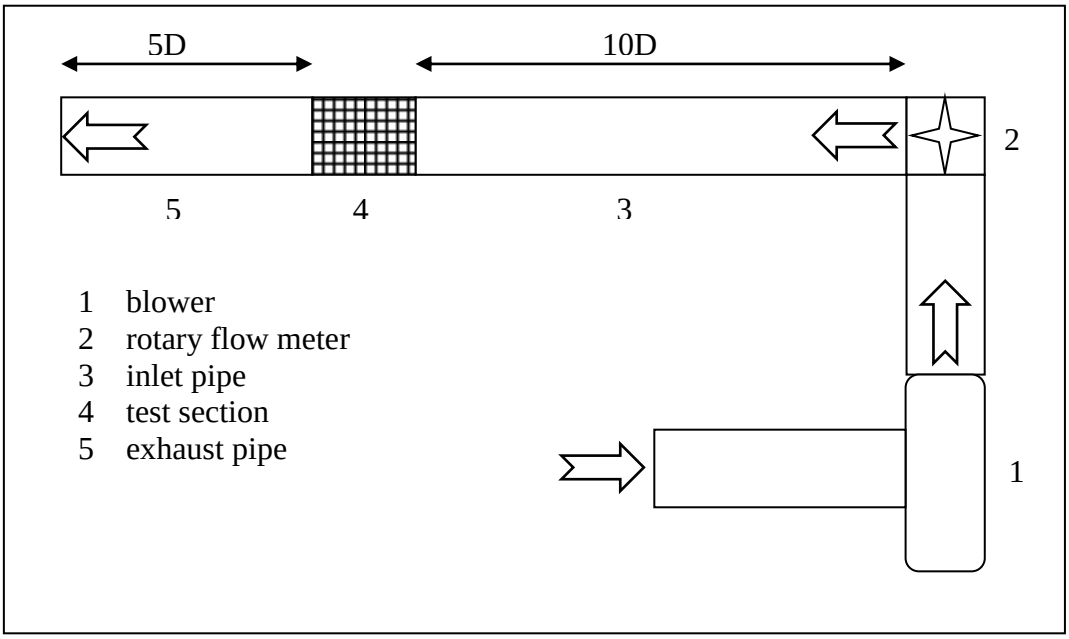

Figure 6-1 Flow Test Apparatus Air Circuit

Figure 6-2 Portable Measurement Devices and Variable AC Transformer

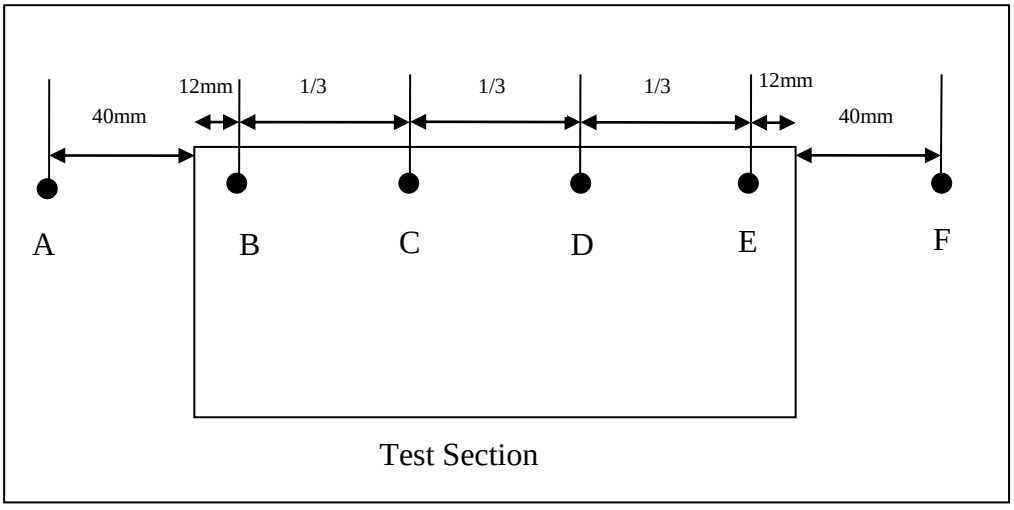

Figure 6-3 Pressure Tap Locations

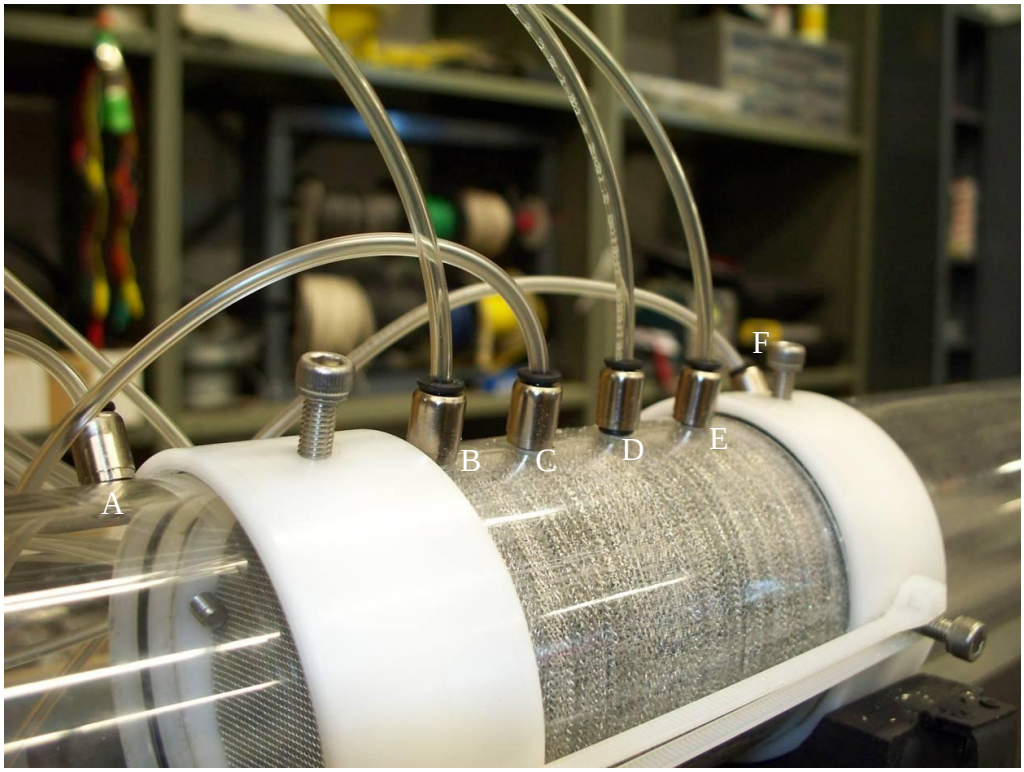

Figure 6-4 Test Section

The entire test apparatus (isolated and in operation) is shown in Figure 6-5 and Figure 6-6. Numbers indicated on the figure below refer to the components of Figure 6-1.

Figure 6-5 Assembled Test Rig

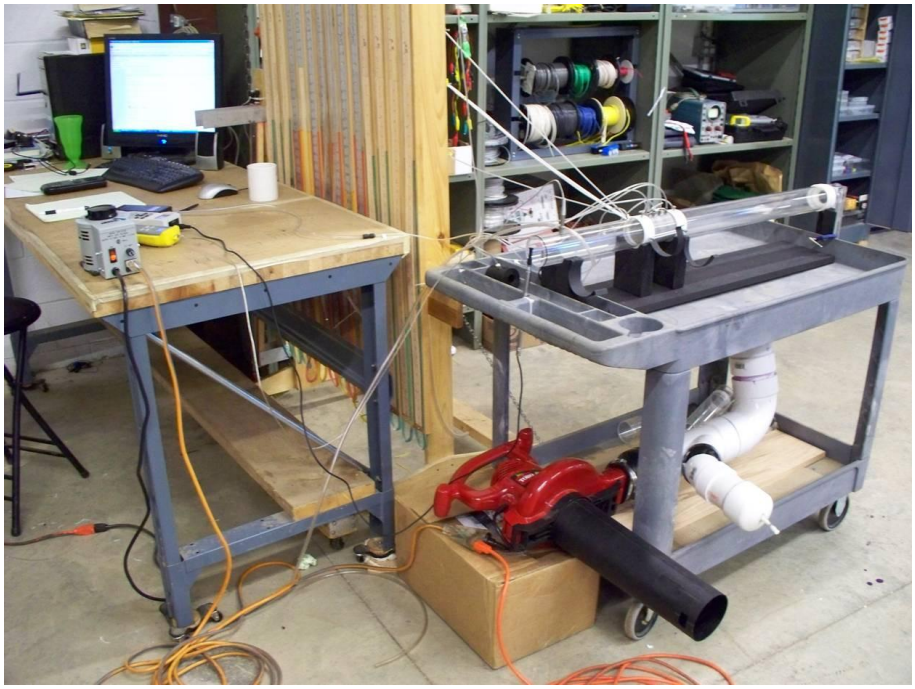

Figure 6-6 Test Rig in Operation

6.4 Flow Test Results

Certain difficulties were encountered during flow testing. Leaks in the seals were noticeable at approach velocities in excess of 0.7m/s. During testing of the Dutch-weave samples, the test section pipe cracked and tests were discontinued. Therefore, results for Dutch-weaves will not be presented. Originally, it was hoped that this testing would provide sufficient data to demonstrate generalized equations for mesh parameters with approach velocities up to 2m/s in a manner similar to Wu et al. [13] but the range was limited to 0.7m/s.

Plotting equation 5.19 with respect to U (superficial velocity) makes it possible to compare the Wu et al. generalized equation with test data. Figure 6-7 illustrates the trends.

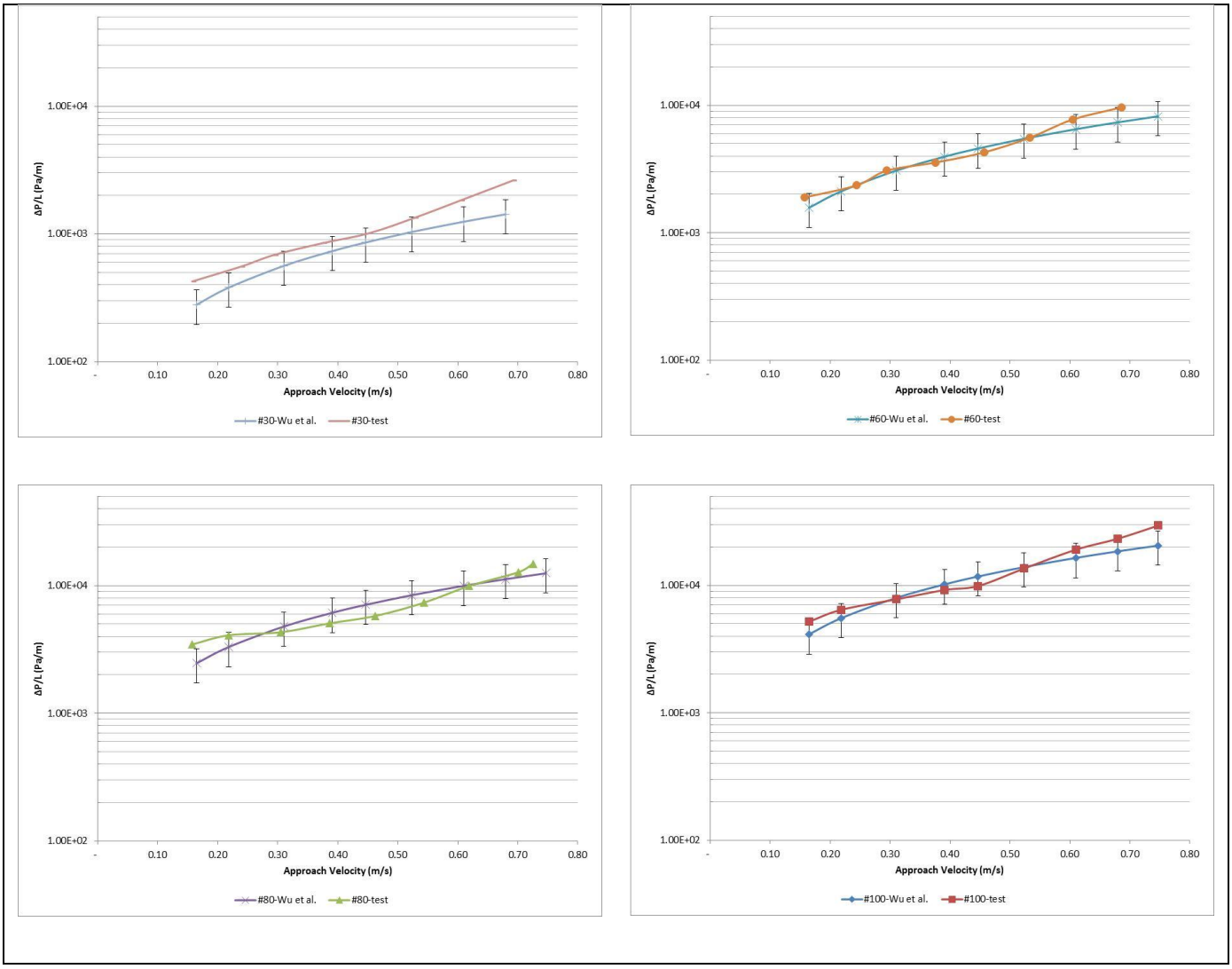

Figure 6-7 Comparison of Test Data with Wu et al.

Ninety-five percent of the data for mesh numbers 60, 80 and 100 lie within +/- 23% of theWu et al. equation while data for the 30 mesh sample is within +/- 48%. Wu et al. indicate that their data fits within +/- 30% of equation 5.19. Although the discrepancy for the 30 mesh sample is significant, overall the results are convincing enough to use the generalized equations for isotropic-weave screens.

6.5 Burst Test Objective

Burst testing demonstrates the tensile strength of the brazed structural sandwich in a manner as similar to real operation as possible. Once a screen type is selected and wafers are produced, it is critical to confirm that the brazed wafer structure is able to withstand the required internal pressure loads at operating temperatures. This is done with a proof test. Required proof test pressure is 3.9MPa for the SolarCAT application. This testing has the added benefit of helping with the development of appropriate brazing procedures.

6.6 Burst Test Apparatus

The proof test pressure for this application is roughly 4MPa. However, to establish the limits of these brazed wafers, a destructive burst test was performed. The burst test fixture (Figure 6-8) accepts 100mm by 100mm samples of varying thickness. The flanges, bolts and feed system are designed to be safe at well over 70MPa but the o-rings fail at roughly 50MPa, which largely exceeds proof test requirements for most gas-turbine recuperators. The pressurized fluid could be water or a compressed gas like nitrogen but water is used for safety reasons.

Figure 6-8 Burst Test Fixture

6.7 Burst Test Results

In order to prepare samples for burst testing, a sintered brick was manufactured as shown in Figure 4-2. Two bricks were manufactured for testing. The first had half of the wire oriented normal to the parallel plates (0-90°) while the all of the second brick's wires are at a 45° angle to the parallel plates (±45°). The bricks were then cut to 100mm by 100mm using wire-EDM as show in Figure 4-3. Then the cubes were cut into a number of parallel wafers 1.9mm thick (Figure 4-4). These wafers are then brazed between two 0.25mm thick plates and burst tested. Optimization of the braze process is a Brayton Energy, LLC trade secret and will not be discussed in this document. Although fine-tuning of the process in still in progress, initial results are shown in Table 6-2. Several samples exceeded the pressure limit of the test fixture and failed to burst. The o-rings fail at 50MPa which puts failure of these samples in excess of 50MPa. Given that proof test pressure for the SolarCAT recuperator application is roughly 4MPa, these samples greatly exceed the requirements. It is felt that once the braze process is mature, most samples should be capable of exceeding 50MPa.

Table 6-2 Burst Test Results

Sample #	Orientation	Failure Pressure	Comment
1	0-90°	3.4MPa	Incomplete bonding
2	0-90°	8.2MPa	Incomplete bonding
3	0-90°	6.9MPa	Incomplete bonding
4	±45°	>50MPa	No failure
5	±45°	6.9MPa	Incomplete bonding
6	±45°	12.4MPa	EDM recast residue (not clean enough)
7	0-90°	>50MPa	No failure
8	±45°	>50MPa	No failure
9	0-90°	30MPa	Valid failure

Failure sites 1A, 1B and 1C in Figure 6-9 demonstrate a failure of either the bond between the wires and plate (braze defect – see Figure 6-10) or failure of the parent metal in the wire (preferable – see Figure 6-12). Site 1D illustrates a bond failure as well as a plate failure. Figure 6-11 shows a typical failure due to brazed joint starvation. Figure 6-13 illustrates a cross-sectional cut through a typical failure.

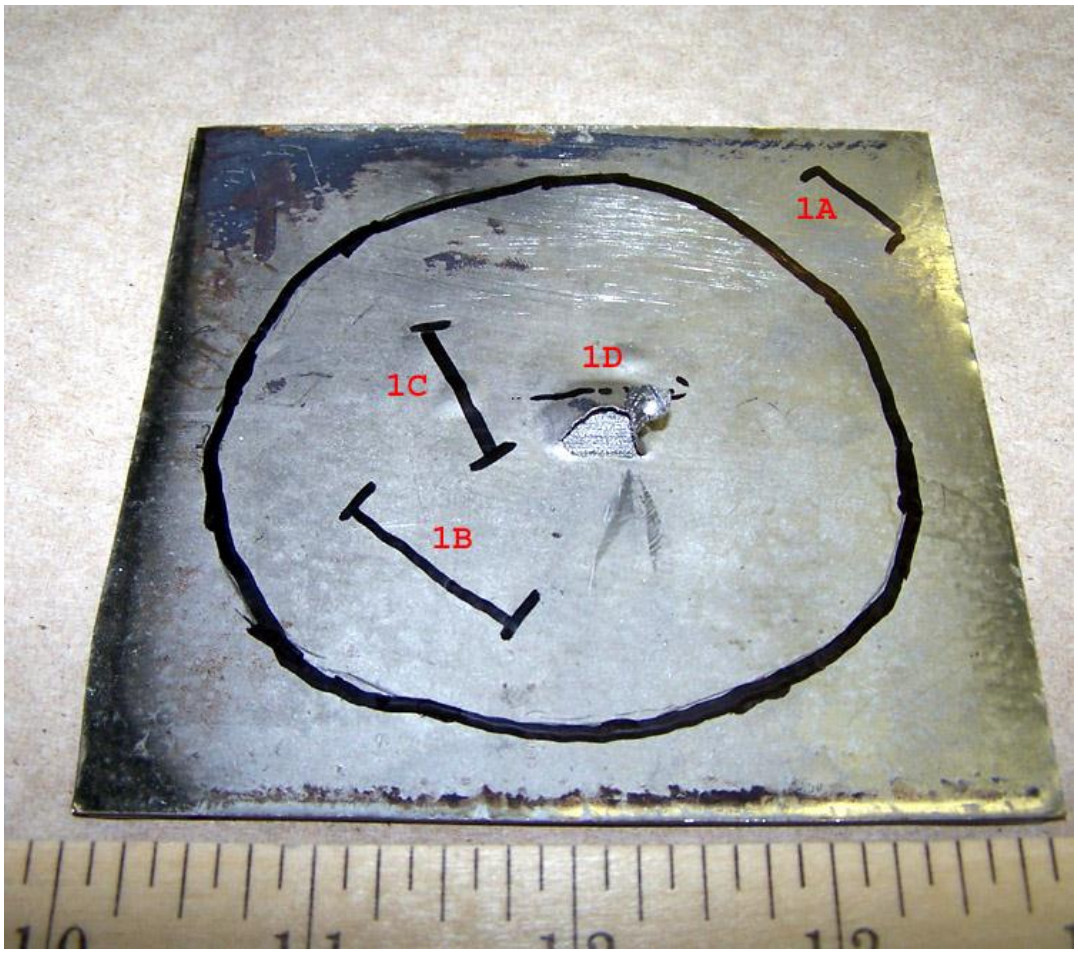

Figure 6-9 Typical Burst Failures

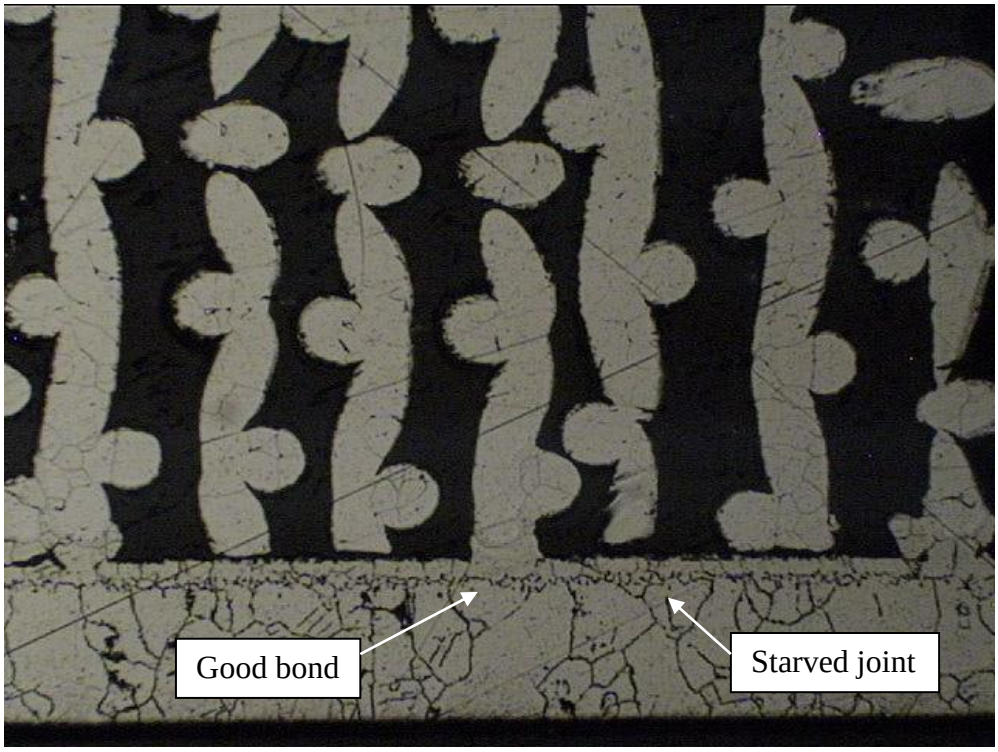

Figure 6-10 Starved Braze Joints (5X scale)

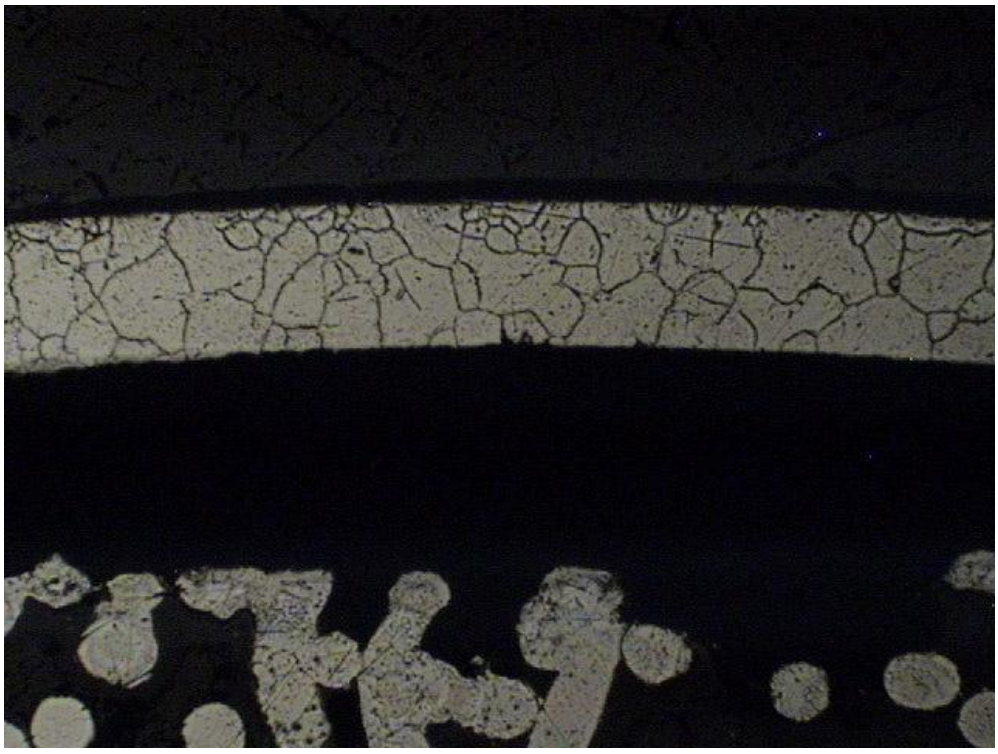

Figure 6-11 Failure at Starved Braze Joint (5X scale)

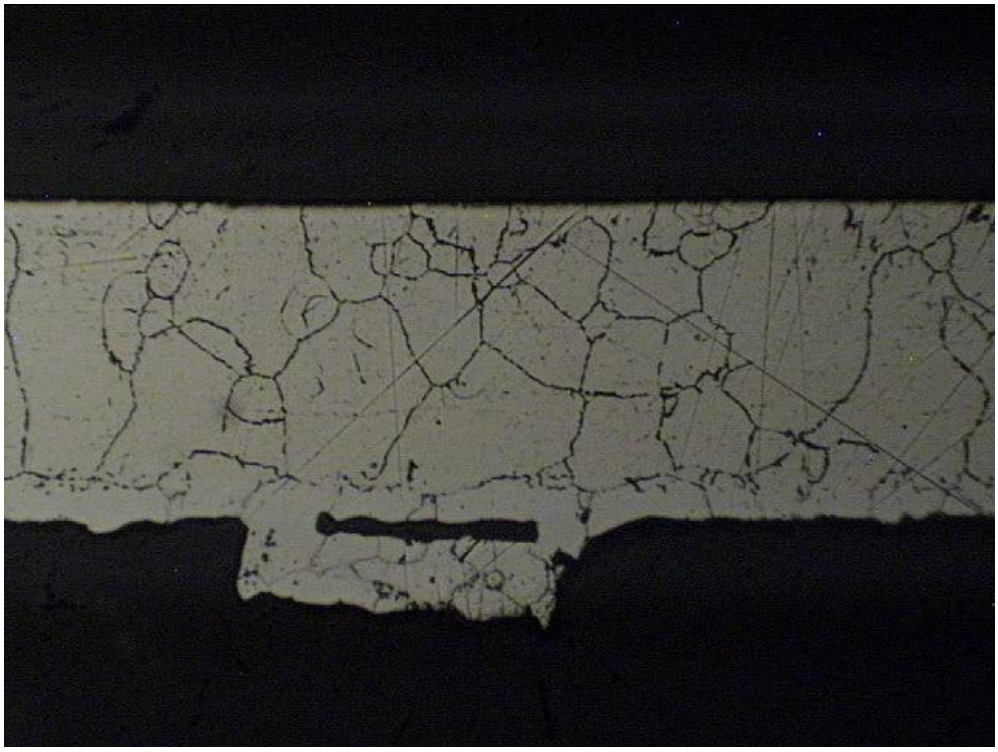

Figure 6-12 Parent Metal Failure (10X scale)

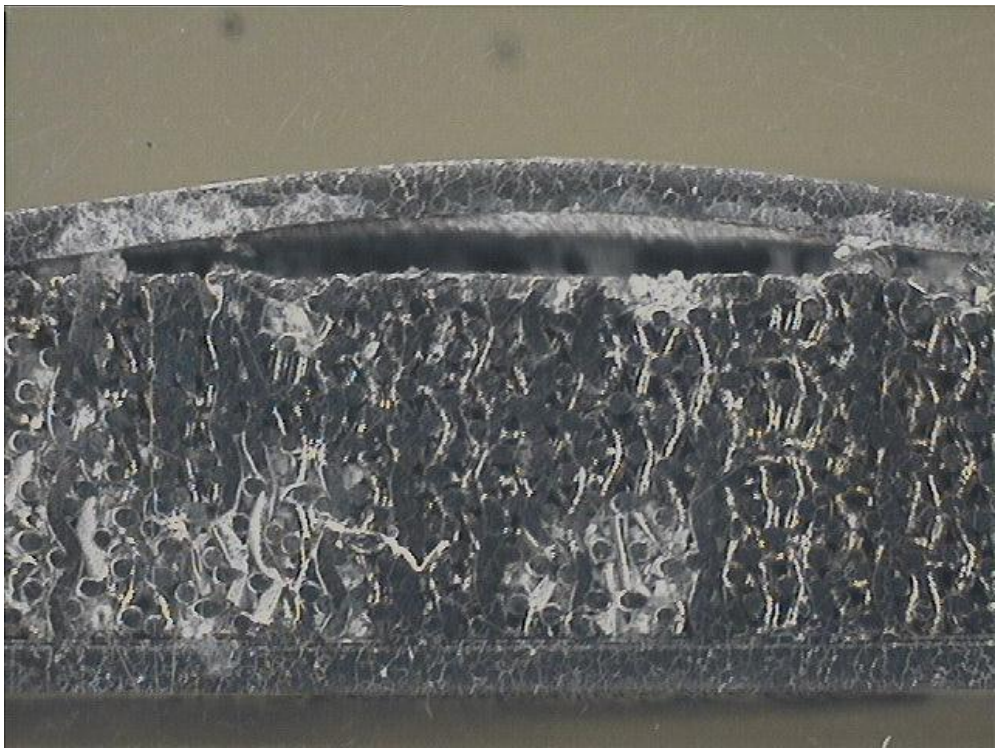

Figure 6-13 Cross-section at Failure Site

7. HEAT EXCHANGER OPTIMIZATION

7.1 Heat Exchanger Performance Program

Brayton Energy's heat exchanger performance program uses the ε-NTU method to assess the performance of a given heat exchanger arrangement. The model respects the process shown in the flow chart in Figure 3-1. The user must input the project specific operating conditions and specify the geometry of internal and external heat transfer surfaces as well as overall dimensions. The program will return performance data such as heat exchanger effectiveness, internal and external pressure losses.

7.2 Inserting the Screen Module

A difficulty that arose when attempting to insert a screen module based on the mathematical representations discussed in chapter 5 was how to address the surface efficiency of the screen as extended surface. Vafai and Kim's model provides a heat transfer coefficient for the total plate surface area exposed to the porous medium. This approach is quite different from that used to define the convective term using an extended surface. The thermal resistance for a typical extended surface is the product of the local heat transfer term, the total wetted extended surface area, including plate area, and the surface efficiency of the selected extended surface.

All equations in the program defining screen performance are a function of the basic geometric terms defining an isotropic-weave screen, mesh number and wire diameter. The user must input these terms and choose to use the screen module for the performance analysis.

7.3 Sizing Optimization

A sizing optimization was performed with Brayton Energy's software modified to accommodate screen as internal extended surface, subject to the constraints listed in section 3.6 and a number of guidelines:

1. Stamped plate tooling should remain largely unaffected. Draw depth can be increased up to 3mm if required (maximum internal channel height of 6.5mm) but matrix width (168mm) must be maintained.
2. Matrix flow length should not exceed 178mm. Anything less will be accommodated by an extended header region.
3. Internal-side heat-transfer medium alloy must remain 347 stainless steel due to oxidation concerns at operating temperatures.
4. Maximum internal pressure loss of 2%.
5. Recuperator must meet or exceed 94%.

Table 7-1 Recuperator Optimization Results

Mesh #	Effectiveness [%]	Pressure Loss - Internal [%]	Number cells	Internal Channel Height [mm]	Flow Length [mm]	Core Height [mm]	Total Matrix Volume [m^3]	Cost Index [%]
43 fpi - ruffled	94.0	<2%	90	0.89	178	600	1.79E-02	100%
30	94.0	<2%	32	1.00	178	190	5.68E-03	39%
60	94.0	2%	32	1.50	150	215	5.42E-03	39%
80	94.0	2%	36	1.50	135	230	5.22E-03	44%
100	94.0	2%	40	1.50	123	235	4.86E-03	49%
60	95.2	2%	35	1.50	178	235	7.03E-03	43%
80	95.8	2%	43	1.5	178	265	7.92E-03	53%
100	96.3	2%	52	1.5	178	300	8.97E-03	64%

The sizing optimization was performed with two separate objectives:

1. For an effectiveness of 94%, minimize the matrix volume and assess cost relative to the current production baseline.
2. Maximize effectiveness within existing tooling constraints (178mm flow length).

The cost index uses the current production recuperator as a baseline. This analysis assumes that labour costs represent 75% of the total cost and will scale linearly with number of unit cells. Material accounts for the remaining 25% with the internal heat-transfer medium accounting for 40% of material costs. It is assumed that screen wafers will be 2 times more costly than folded fin.

The first row of Table 7-1 illustrates certain details of the current production recuperator and assigns a cost index of 100% to the baseline configuration. The next four rows illustrate the minimum volume heat-exchangers using the four mesh numbers tested as internal heat-transfer medium, and assuming a compression factor of 0.75 for the sintering operation to produce mesh bricks. The #30 mesh configuration does not fully use the pressure loss budget of 2% but offers the smallest overall core height and lowest cost index.

The last three rows illustrate configurations that leave stamped plate tooling unchanged (flow length of 178mm) and maximise effectiveness. The #100 mesh configuration offers the best performance if one assumes that the cost benefits due to higher effectiveness overwhelm (section 1.2.2) the relative cost differences for the last three configurations. Based on these results, a #100 mesh brick was manufactured for burst testing to confirm feasibility for the SolarCAT recuperator application.

8. CONCLUSIONS

The objectives of this study were to compare potential techniques for achieving highly compact heat-transfer media, selection of an appropriate medium to replace the internal folded fin of the SolarCAT recuperator, and to demonstrate feasibility of the chosen medium through appropriate testing. This chapter outlines the most important tasks in the process to achieve the objectives of the study and provide input for further research.

8.1 Review of Compact Heat-Transfer Media

For plate-fin heat-exchangers, fin-folding is a well-developed process that can accommodate the vast majority of common applications. However, in certain situations, the design of a heat-exchanger can be limited by the ability to manufacture a sufficiently compact heat-transfer medium using this process. Several alternative solutions were reviewed and discussed.

Spherical packed beds are a simple solution to achieve high specific surface areas and small hydraulic diameters but small contact regions between adjacent spheres (almost point-contact) create limitations. Effective thermal conductivities lie in the range of 10% to 15% and the ability to withstand internal pressures is similarly affected. Micro-tubes are another potential solution but they also would suffer from limitations to effective thermal conductivity and have a significant cross-sectional area for longitudinal conduction that can lead to significant performance decrements in the proposed configuration.

Sandwich structures made of lattice frame materials, Kagome structures, and textiles were reviewed. The first two solutions present manufacturing challenges to achieve the desired range of hydraulic diameters but the textile solution proves to be worthy of further investigation. The textiles can be tailored to achieve a wide range of hydraulic diameters, porosity, specific surface area and effective thermal conductivity (up to 23% for isotropic plain weaves and up to 78% for anisotropic plain weaves).

Metal foams are a relatively inexpensive solution that can be produced in a large variety of materials with widely varying pore sizes and densities. The foams have an interconnected network of solid struts with random orientation that leads to relatively low values of effective thermal conductivity (2% to 6%) and low tensile strength limits.

Various micro-machining techniques were explored. Although most techniques are able to achieve very small hydraulic diameters, the material removal techniques all have the same problem that affects micro-tubes. As hydraulic diameters decreases, the relative cross-sectional area for longitudinal thermal conductivity increases. Also with small hydraulic diameters is an increase in pressure loss which encourages shorter flow lengths, leading to increased decrements associated with axial conduction losses. As a result, textiles sandwiches were retained for further study.

8.2 Selection of Mathematical Representations

A literature search was performed to identify appropriate mathematical models to properly represent the thermal/fluid characteristic of textiles wafers for use in the SolarCAT recuperator. Xu and Wirtz [8] present an excellent physical model that defines basic geometric screen parameters and develops equations for porosity, specific surface area and effective thermal conductivity. The relatively long flow (>150mm) path through the proposed screen wafers requires a model for fully-developed forced convective flow between parallel plates. Vafai and Kim [18] present an exact solution for this situation. Wu et al. [13] attempt to create a generalized equation for screen friction factors that covers all weave types. They found that a single equation for each type of weave is required and present five equations for friction factor as a function of a porosity-modified Reynolds number.

The Wu et al. equation for plain weaves was modified to reflect $\Delta P/L$ as a function of U (superficial velocity) and U^2. From this modified form, it was possible to extract equations for permeability and Forchheimer coefficient that were then used in the Vafai and Kim model along with effective thermal conductivity and other geometric terms from Xu and Wirtz. The resulting equations were integrated into Brayton Energy's proprietary heat-exchanger performance program. Optimization of this performance program lead to the decision to produce wafers of #100 mesh 100mm by 100mm by 1.9mm thick.

8.3 Testing

Flow testing was conducted to confirm that the generalized equation for plain weaves presented by Wu et al. was representative for potential screen geometries over superficial velocities in the range of interest for this application. It was found that for velocities up to 0.7m/s the data fell within the ±30% suggested as appropriate by the authors.

The #100 mesh wafers were brazed between two 0.25mm stainless steel sheets and destructively tested to assess their tensile strength. Although optimization of the braze parameters was not completed, it was found that many samples survived exposure to internal pressures in excess of 50MPa.

8.4 Final Word and Recommendations

This study found that the use of sintered screen wafers to replace the internal folded fin of the SolarCAT recuperator would have advantages over the current design with respect to both overall recuperator effectiveness, size, and cost. Textile structures can be tailored to have wide range of fluid and heat-transfer properties depending on the application. The manufacturing process is relatively simple and could be cost-effective for high-volume production.

Salimijazi et al. [20] demonstrate the ability to deposit a “skin” on the surface of a nickel foam substrate using wire-arc spraying to produce a heat-exchanger. Given that materials and

preparation for the braze process represent a significant portion of unit cell cost, replacing that process with a spray process that can be automated seems beneficial. Perhaps a spray process such as HVOF (High Velocity Oxygen Fuel), plasma spray, or cold spray could be used to directly apply a coating to the screen wafer and entirely replace the braze process. However, given the internal pressures within the sandwich structure, proper assessment of bond strength would be critical. Also, it would be important to verify if the particles penetrate the surface and create additional obstruction for the flow.

REFERENCES

[1] **Cohen, H, Rogers, G.F.C. and Saravanamuttoo, H.I.H.** *Gas Turbine Theory.* Essex, England : Longman Group Limited, 1996.

[2] **Bohn, Dieter.** *Micro Gas Turbine and Fuel Cell - A Hybrid Energy Conversion System with High Potential.* Neuilly-sur-Seine, France : RTO, 2005. RTO-EN-AVT-131, Paper 13.

[3] **Lymberopoulos, N.** *Microturbine and their Application in Bio-energy.* Pikermi Attiki, Greece : Centre for Renewable Energy Sources, 2004. NNE5-PTA-2002-003/1.

[4] **Shah, R.K. and Sekulic, D.P.** *Fundamentals of Heat Exchanger Design.* Hoboken, New Jersey : John Wiley & Sons, Inc., 2003.

[5] **Kays, W.M. and London, A.L.** *Compact Heat Exchangers.* New York : McGraw-Hill, Inc., 1984.

[6] *The effects of topology upon fluid-flow and heat-tranfer within cellular copper structures.* **Tian, J., et al.** s.l. : International Journal of Heat and Mass Transfer, 2004, Vol. 47.

[7] *Metal foams as compact high performance heat exchangers.* **Boomsma, K., Poulikakos, D. and Zwick, F.** s.l. : Mechanics of Materials, 2003, Vol. 35.

[8] **Xu, J. and Wirtz, R.A.** In-Plane Effective Thermal Conductivity of Plain-Weave Screen Laminates. *IEEE Transactions on Components and Packaging Technologies.* 2005, Vol. 25, 4.

[9] Guide to Compact Heat Exchangers. *Scribd.* [Online] [Cited: 09 14, 2009.] http://www.scribd.com/doc/9188918/Compact-Heat-Ex-Changers.

[10] *Fluid flow through woven screens.* **Armour, J.C. and Cannon, J.N.** 3, s.l. : AIChE Journal, 1968, Vol. 14.

[11] *Friction factor determination for flow through finite wire-mesh woven-screen matrices.* **Sodré, J.R. and Parise, J.A.R.** s.l. : Journal of Fluids Engineering, 1997, Vol. 119.

[12] *Wall Effect in Packed Columns.* **Mehta, D. and Hawley, M.C.** 2, s.l. : I&EC Process Design and Development, 1969, Vol. 8.

[13] *Measurement and correlation of hydraulic resistance of flow through woven metal screens.* **Wu, W.T., et al.** s.l. : International Journal of Heat and Mass Transfer, 2005, Vol. 48.

[14] *Thermal/fluid characteristics of isotropic plain-weave screen laminates as heat-exchange surfaces.* **Park, J.W., Ruch, D. and Wirtz, R.A.** s.l. : American Institute of Aeronautics and Astronautics, Inc., 2002, Vol. 0208.

[15] *In-plane effective thermal conductivity of plain weave screen laminates with arbtrary weave parameters.* **Xu, J. and Wirtz, R.A.** s.l. : ASME-JSME Thermal Engineering Joint Conference, 2003.

[16] *Thermal/fluid characteristics of 3-D woven mesh structures as heat exchanger surfaces.* **Wirtz, R.A., et al.** 1, s.l. : IEEE Transactions on Components and Packaging Technologies, 2003, Vol. 26.

[17] *The effective thermal conductivity of wire screen.* **Li, C. and Peterson, G.P.** s.l. :

International Journal of Heat and Mass Transfer, 2006, Vol. 49.

[18] *Forced convection in a channel filled with a porous medium: an exact solution.* **Vafai, K. and Kim, S.J.** s.l. : Journal of Heat Transfer, 1989, Vol. 111.

[19] *Experimental determination of permeability and inertia coefficients of mechanically compressed aluminum porous matrices.* **Antohe, B.V., et al.** s.l. : Transactions of the ASME - Journal of Fluids Engineering, 1997, Vol. 119.

[20] *Spray forming of metal foam heat exchangers.* **Salimijazi, H.R., et al.** Volterra, Italy : Interdisciplinary Transport Phenomena VI: Fluid, Thermal, Biological, Materials and Space Sciences, 2009. ITP-09-81.